
^{13}C HYPERPOLARIZATION WITH NITROGEN-VACANCY CENTERS IN MICRO- AND NANODIAMONDS FOR SENSITIVE MAGNETIC RESONANCE APPLICATIONS

PREPRINT

Rémi Blinder^{*1}, Yuliya Mindarava¹, Martin Korzeczek², Alastair Marshall^{†3}, Felix Glöckler^{‡4}, Steffen Nothelfer^{§4}, Alwin Kienle⁴, Christian Laube⁵, Wolfgang Knolle⁵, Christian Jentgens⁶, Martin B. Plenio^{2,7}, and Fedor Jelezko^{1,7}

¹Institute for Quantum Optics, Albert-Einstein Allee 11, Ulm University, 89081 Ulm, Germany

²Institute of Theoretical Physics, Albert-Einstein Allee 11, Ulm University, 89081 Ulm, Germany

³NVision Imaging Technologies GmbH, 89081 Ulm, Germany

⁴Institute for Laser Technologies in Medicine and Metrology at the University of Ulm (ILM), Helmholtzstr. 12, 89081, Ulm, Germany

⁵Leibniz Institute of Surface Engineering, Leipzig 04318, Germany

⁶Pureon AG, Kreuzlingerstrasse 1, 8574 Lengwil, Switzerland

⁷Centre for Integrated Quantum Science and Technology (IQST), Ulm 89081, Germany

ABSTRACT

Nuclear hyperpolarization is a known method to enhance the signal in nuclear magnetic resonance (NMR) by orders of magnitude. The present work addresses the ^{13}C hyperpolarization in diamond micro- and nanoparticles, using the optically pumped nitrogen-vacancy center (NV) to polarize ^{13}C spins at room temperature. Consequences of the small particle size are mitigated by using a combination of surface treatment improving the ^{13}C relaxation (T_1) time, as well as that of NV, and applying a technique for NV illumination based on a microphotonic structure. Monitoring the light-induced redistribution of the NV spin state populations with electron paramagnetic resonance, a strong polarization enhancement for the NV spin state is observed in a narrow spectral region corresponding to about 4% of these defect centers. By combining adjustments to the ‘PulsePol’ sequence and slow sample rotation, the NV- ^{13}C polarization transfer rate is improved further. The hyperpolarized ^{13}C NMR signal is observed in particles of 2 μm and 100 nm median sizes, with enhancements over the thermal signal (at 0.29 T magnetic field), of 1500 and 940, respectively. The present demonstration of room-temperature hyperpolarization anticipates the development of agents based on nanoparticles for sensitive magnetic resonance applications.

Keywords Nanodiamonds, nuclear hyperpolarization, nitrogen-vacancy center, magnetic resonance, MRI

Introduction

As a technique improving the sensitivity of Nuclear Magnetic Resonance (NMR) and Magnetic Resonance Imaging (MRI), hyperpolarization is widely explored for enhancing the acquisition of the nuclear precession signal.¹ Besides its applications in medical imaging,^{2,3} it holds the promise of benefiting multiple research fields including metabolomics,⁴ drug screening and monitoring,^{5,6} the study of proteins,⁷ nano/mesoporous systems⁸ or battery materials.⁹ Signal enhancements by above 4 orders of magnitude were demonstrated in the work from Ardenkjær-Larsen *et al.* in 2003,¹⁰

*To whom correspondence should be addressed: remi.blinder@uni-ulm.de

†Present address: Quise GmbH, Am Hölzersbach 7, 66113 Saarbrücken, Germany

‡Present address: Sensific GmbH, 89081 Ulm, Germany

§Present address: Hensoldt, Wörthstraße 85, 89077 Ulm, Germany

employing the method, nowadays known as dissolution Dynamical Nuclear Polarization (dissolution DNP), which enabled *in-vivo* imaging of metabolic processes.¹¹ Despite these accomplishments, alternative concepts are being investigated, with the prospect of reducing hardware cost and complexity (that are both elevated in dissolution DNP, due to the use of cryogenics) or, to bring magnetic resonance signal boosts to new systems. To circumvent the need for cryogenic temperatures, yet achieve high nuclear signal enhancements, a proposed approach is the use of DNP protocols with electrons that are initialized out-of-equilibrium in a spin state with above-thermal polarization. Early on, in 1990, this was demonstrated by Henstra *et al.*,¹² who used the photoexcited state of pentacene molecules in naphthalene to produce high nuclear spin polarization at room temperature. In recent developments, the same method was successfully applied to polarize other matrices,^{13,14} and its combination with Nuclear Overhauser Effect enhancement in the liquid state was demonstrated, allowing for polarization of external substances.^{15,16}

An interesting prospect in terms of novel applications of DNP is the generation of hyperpolarization within nanoparticles (<200 nm). This stems from the following reasons: 1) such nanoparticles can diffuse efficiently by circulation in the blood flow,¹⁷ making them candidate for the application as MRI tracers and 2) owing to the high surface-to-volume ratio, they could play the role of renewable source of polarization for external substances. The possibility of performing MRI acquisitions enhanced by hyperpolarization was demonstrated with ¹³C in diamond^{18,19} or ²⁹Si in silicon²⁰ nanoparticles, both polarized from thermally polarized endogenous spin defects in a cryogenic environment, at liquid Helium temperatures. Although this scheme performs well under the cryogenic setting, it shows limited efficiency under ambient conditions.

Nanodiamonds attract interest due to several factors, that is, the long ¹³C spin polarization lifetime (T_1) in diamond,²¹ the good biocompatibility,²² and the possibility of producing single-crystalline nanoparticles with lattice properties similar to bulk.²³ Diamond can also host a wide variety of paramagnetic defects²⁴ that can be used for DNP. One example is the substitutional nitrogen or P1 center ($S = 1/2$),²⁵⁻²⁷ which is incorporated during growth. Specifically in nanodiamonds, near-surface spin defects,^{28,29} have also been employed.^{18,19,30,31} Finally, hyperpolarization was demonstrated using the nitrogen-vacancy center (NV), either in bulk crystal³²⁻³⁵ or diamond powder (>1 μ m particles).³⁶⁻³⁸ DNP techniques relying on the NV spin, $S = 1$, draw on the essential capability that it can be initialized to a high degree (up to 92%) into the $m_s = 0$ state,³⁹ upon excitation with short pulses of green light, at arbitrary magnetic field and ambient conditions. By combining optical pumping with dynamical nuclear polarization, it becomes possible to transfer the spin polarization generated on the NV to surrounding nuclei. Harnessing NV as a polarization source holds the potential to push the boundaries of conventional DNP methods. This approach could potentially achieve high levels of nuclear polarization, without the requirement of cryogenic temperatures.

However, material and DNP protocols must be optimized in order to fulfill requirements of using color centers in nanoparticles, such as NV in nanodiamonds. Previous attempts to hyperpolarize ¹³C spins from NV in diamond nanocrystals (<200 nm) resulted in only a very low degree of nuclear polarization.^{37,38} In this work, we address the primary challenges affecting the efficiency of nuclear hyperpolarization in nanodiamonds. First, we mitigate the impact of surface magnetic noise on ¹³C relaxation time by appropriate surface treatment. Second, we enhance NV initialization by improving sample illumination. Furthermore, we increase the number of NV that are involved simultaneously in polarization transfer to nuclear spins by adjusting parameters in a DNP sequence (PulsePol)⁴⁰ to enhance its robustness to the orientation-induced broadening of the NV spectrum in powder samples. Last, we implement slow sample rotation ($\leq 25^\circ/s$) to bring different subsets of NV into the excitation region of the adapted DNP sequence and cycle through all of them. Thanks to these improvements, we achieve efficient polarization transfer from NV to ¹³C spins within diamond particles of 2 μ m and 100 nm typical sizes, resulting in NMR signal enhancements over the thermal signal of 1500 and 940, respectively, at the polarization field of about 0.29 T.

Results and discussion

In this work, we use diamond powders from Pureon AG (Lengwil, Switzerland) with median sizes of about 2 μ m and 100 nm (see Supporting Information (SI), section S1 for size distribution parameters). Substitutional nitrogens (P1 centers) are converted into NV by high-energy electron irradiation and annealing, as described in a previous work.⁴¹ In this process, oxidation at high temperature (620 °C) in air is performed to remove graphitic residues.⁴² Besides the resulting NV concentrations, given in Table 1, we also consider the ¹³C spin-lattice relaxation time ($^{13}\text{C}T_1$), which is a crucial parameter for hyperpolarization experiments. The $^{13}\text{C}T_1$ determines not only the attainable level of nuclear hyperpolarization but also the duration allowed between hyperpolarization and signal detection in the investigated sample. While microdiamonds are expected to exhibit a $^{13}\text{C}T_1$ as in bulk crystals of similar defect composition, the spin-lattice relaxation in nanodiamonds (<200 nm) typically shows contribution related to surface spins (dangling bonds etc.).⁴³ In such small particles, in order to prolong the $^{13}\text{C}T_1$, it is thus important to work towards suppression of the surface magnetic noise. Besides the air oxidation, our 100 nm particles were as well treated with a three-

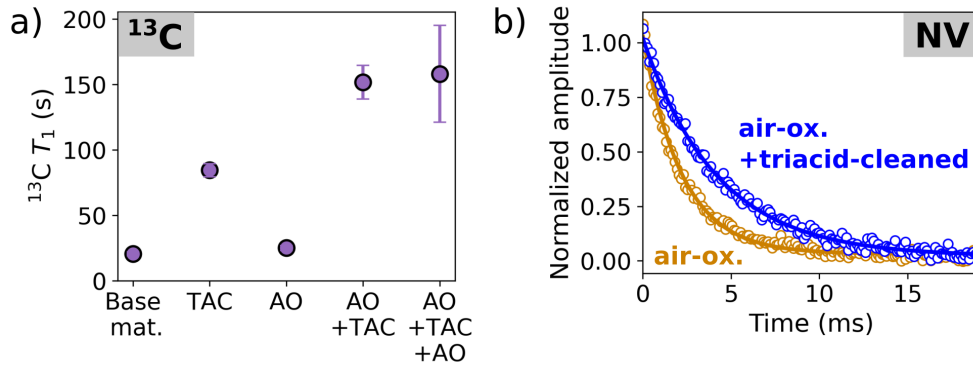


Figure 1: Improving the spin longitudinal relaxation times of ¹³C, NV by surface treatment of nanodiamonds (100 nm) reducing contributions to broadband magnetic noise a) Evolution of the ¹³C T_1 measured in NMR ($B = 7.05$ T) following treatments of the base commercial material: air-oxidation (AO), triacid cleaning (TAC), or combinations (AO+TAC and AO+TAC+AO). Both combinations lead to an about seven-fold improvement over the relaxation time in the original material b) For the electron-irradiated and annealed sample, containing NV, comparison of the ^{NV} T_1 taken on the $m_S = 0$ to $+1$ transition at $B = 0.24$ T, following application of a laser pulse. Solid lines are exponential decay fits, providing ^{NV} $T_1 = 2.20(3)$ ms and $4.23(7)$ ms following the air-oxidation (AO) and the combined (AO+TAC) treatment, respectively.

acid mixture, as detailed in Experimental section. To validate this approach, we investigated the NMR ¹³C T_1 at different stages of treatment of the commercial nanodiamonds. The data in Figure 1a was acquired at $B = 7.05$ T magnetic field, remarkably providing evidence that removal of relaxation-inducing sources is better achieved through the combination of air-oxidation (AO) and triacid cleaning (TAC), rather than by performing each treatment separately. The combination (AO+TAC) indeed leads to ¹³C $T_1 = 152(12)$ s at 7.05 T, which constitutes an improvement by over a factor of seven with respect to the base commercial material (¹³C $T_1 = 21(1)$ s). That improvement is dominantly accounted for by the triacid cleaning (leading alone to an about four-fold increase). We explain these results as follows: air-oxidation achieves a first part of the required surface cleaning, by efficiently removing the surface graphite and the related dangling bonds. The triacid cleaning achieves an important second part, by removing paramagnetic metallic residues. The iron element could be detected by X-ray photoemission spectroscopy (XPS) on smaller nanodiamonds from the same manufacturer, thus constitutes the most likely origin of the magnetic noise (see SI, section S2.4). To investigate further the impact of the acid treatment step, we measure the longitudinal relaxation time of NV (^{NV} T_1) by pulsed electron paramagnetic resonance (EPR), on the air-oxidized sample, before and after acid cleaning. From the results shown in Figure 1b, it can be seen that the combined treatment prolongs ^{NV} T_1 by more than a factor of two, compared to air oxidation alone (Table 1). We correlate this observation with the disappearance of a broad (~ 3000 G) signal in X-band EPR, that we attribute to the removal of the iron impurities (SI, section S2.1). Here, observing the short ^{NV} T_1 before the treatment with acid as in Figure 1b is a telltale sign of magnetic noise extending in the high-frequency (\sim GHz) range, thereby impacting the relaxation of spins having comparable or lower resonant frequencies.⁴⁴ Last, although air-oxidation and triacid cleaning might provide a different balance of functional groups on the surface, this (possible) difference does not seem to affect the longitudinal relaxation, as visible from Figure 1a. Indeed, after applying again air oxidation (AO+TAC+AO), no detectable change in ¹³C T_1 is observed.

We turn our attention to the process of NV initialization by optical pumping, which is yet another prerequisite to performing (efficient) hyperpolarization. To monitor this process, we use again EPR. In addition to being a valuable tool for determining the concentration, T_1 and T_2 times of NV, EPR allows precise tracking of the redistribution of the NV spin state populations under illumination.⁴⁵ In fact, although EPR spectra of optically polarized NV ensembles in powder samples have been reported,^{37,46} performing homogeneous illumination of NV in macroscopic quantities of micro- and nanodiamond remains a challenge, owing to the strong light scattering created by the difference in refractive index between the diamond ($n = 2.4$, at 532 nm wavelength) and its surroundings. To overcome this issue, we couple light into a structure of closely packed waveguides forming an array, in which the diamond powder is embedded together with a solution of ethylcinnamat acting as buffer between the structure and the diamond. The details of the illumination protocol are presented in SI, section S3.

In Figure 2 is shown the NV spectrum measured with pulsed EPR for the 2 μ m particles, using the microstructured waveguide array for illumination with green light (532 nm). The spectrum shows a broad structure, spreading equally on each side of the $g \sim 2$ electron resonance field (on which the signal from P1 centers, seen in Figure 2, is centered as

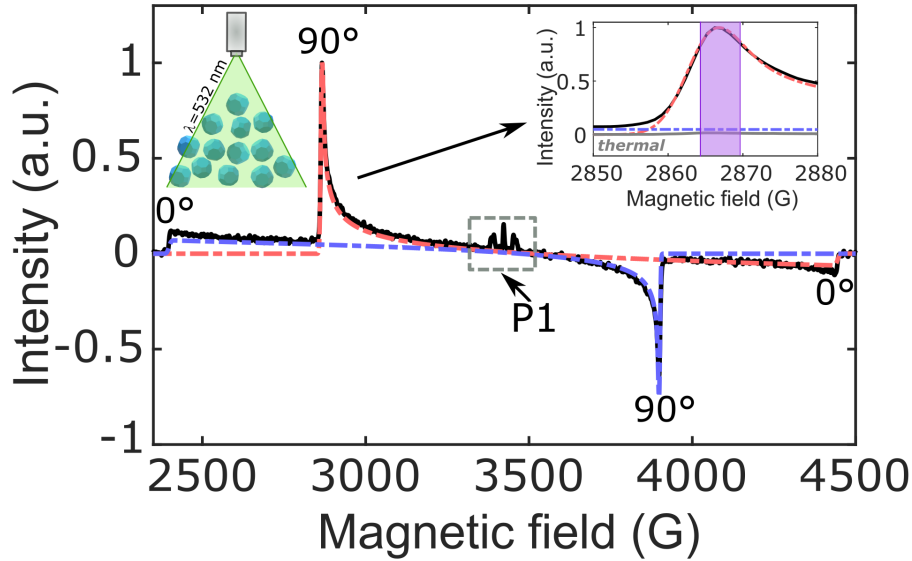


Figure 2: Pulsed X-band EPR spectrum under illumination, for the sample of 2 μm particles. The experimental data (solid black line) was acquired by echo detection following a 700 μs laser pulse, using the microwave frequency $\nu = 9.59$ GHz. Dashed red and blue lines are simulated spectra for the two separate spin transitions of NV fitting the experimental spectrum (see SI, sect. S3.2 for the description of the simulation). The resonance positions for NV having their axis either aligned (0°) or perpendicular (90°) to the magnetic field, locate at the spectrum extremities and on the intense peaks, respectively (as indicated). Besides NV, the P1 spectrum appears in the central part. The right inset shows a zoom on the low-field peak of the optically polarized spectrum and its comparison to the acquired thermal signal (grey), showing here a 85-fold enhancement with illumination. The shaded blue area in the right inset highlights a region corresponding to a range of $\Delta = (2\pi)15$ MHz width in the frequency domain, in which transitions for about 4% of all NV are addressed.

well). Considering the large value of the zero-field splitting for NV ($D = 2.87$ GHz), the important inhomogeneous broadening arises in powder samples as the axis of NV within randomly oriented diamond particles has uniform distribution across the complete solid angle. In the dark, the spectrum has a characteristic structure, known as the Pake doublet,⁴⁷ showing two intense positive peaks, corresponding to NV being oriented perpendicular to the magnetic field.^{46,48} Under illumination (Figure 2), the NV spectrum exhibits positive enhancement in the low-field region and negative enhancement in the high-field part (thus a zero-crossing near the $g = 2$ resonance). These changes result from the redistribution of populations in the NV ground spin state, here induced by optical pumping. Importantly, in EPR, the signal scales with the difference in population $(\Delta\rho)_{\text{NV}}$ between the two states involved in the spin transition. Thus, by measuring in a chosen spectral region in the dark, and comparing the signal to that observed under illumination, the population difference ratio $(\Delta\rho)_{\text{NV}}/(\Delta\rho)_{\text{NV,dark}}$ can be estimated (SI, section S3.4). In the spectral region in Figure 2 in which the highest spectral intensity is attained, that is at the low field peak ($B \approx 0.287$ T), we determine $(\Delta\rho)_{\text{NV}}/(\Delta\rho)_{\text{NV,dark}} = 46$ and 61, following a 400 μs laser pulse (used later on for NV initialization), for the samples containing 2 μm and 100 nm particles, respectively (Figure S11 in SI). The 100 nm particles being more efficient light scatterers, the mass to be exposed to the laser beam was decreased two-fold in order to keep similar illumination conditions. Considering that the signal intensity in the dark is governed by the Boltzmann statistics (details in SI, section S3.4), the *absolute* population difference is estimated as $(\Delta\rho)_{\text{NV}} \approx 3\%$ (2.4 and 3.2%, respectively).

We now focus on the DNP sequence used for NV-¹³C polarization transfer. Considering that the NV spectrum spans over an extended spectral range (Figure 2), corresponding in the frequency domain to over several GHz, it appears essential to carefully select the protocol for NV-¹³C polarization transfer, and of utmost importance to look for DNP sequences offering a high degree of robustness to existing parameter inhomogeneities. First, the polarization transfer sequence should reduce the impact of the strong spectral broadening, by working over a wide range of frequency detunings for NV. Second, efficient operation in the presence of Rabi drive imperfections is also desired - to alleviate inhomogeneities in the MW field or in the NV transition dipole. In this work, we consider the PulsePol sequence, represented in Figure 3a⁴⁰ and its variant, shown in Figure 3b.⁴⁹ We highlight a notable difference to the integrated solid effect (ISE) sequence, which was first introduced by Henstra *et al.*,¹² later used in microdiamonds^{36,37} and

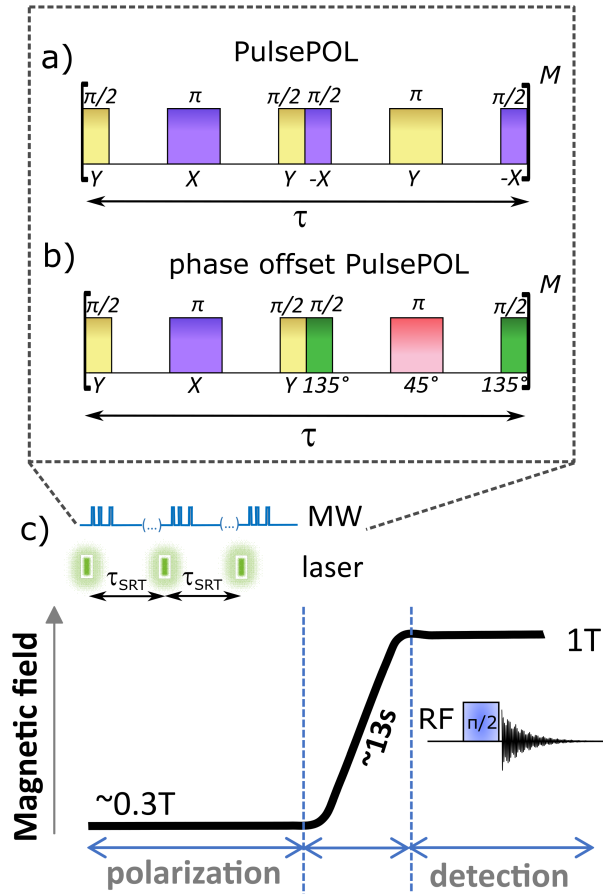


Figure 3: Sequences and timings. a) Conventional PulsePol sequence and b) phase-offset variant. Both the sequences in a) and b) include equal delays between the π and $\pi/2$ pulses. By adjusting these waiting times, one varies the interval τ (length of the 6-pulse block), which determines the resonant condition for polarization transfer. The represented pattern is repeated M times, so that $M \times \tau$ is the duration of the interaction with the nuclear spins. c) Illustration of the hyperpolarization protocol. One polarization cycle consists in performing NV initialization by a laser pulse and polarization transfer using one of the sequences in (a,b). The cycle is repeated at regular intervals (with a period τ_{SRT}) in order to build up nuclear polarization. For NMR detection, the magnetic field is ramped up to 1 T, which takes about 13 s, and the ¹³C signal is acquired *in-situ*

compared to PulsePol.⁴⁰ PulsePol (or its variant) uses discrete pulses, while the ISE exploits the dynamics of the electron-nuclear transitions occurring during a long, continuous pulse.^{50,51} With PulsePol, the peak microwave power determines the NV spectral range (Δ_{pol}) in which NV-¹³C polarization transfer is effective, that is $\Delta_{pol} \sim \Omega_1$ where Ω_1 is the Rabi frequency for NV. This property brings some benefits with respect to the speed of polarization: in the range covered by Δ_{pol} , the NV are addressed in parallel, while sequences such as the ISE manipulate them sequentially, by action of a frequency (or field) sweep. As Ω_1 has no theoretically imposed limit, it is sensible to operate the instrumentation at the highest output power. Working with a 40 W amplifier guarantees in our system that the Rabi frequency of NV is $\Omega_1 = (2\pi)10.5$ MHz. We use this microwave source to drive NV that are oriented at 90° to the magnetic field. This allows enhancing the fraction of centers that are participating to the polarization dynamics, due to the larger solid angle that is covered along the equator of a sphere. For these NV, we choose to drive the transition that shows the highest NV polarization enhancement under illumination, that is the low field peak, visible at $B = 0.287$ T in Figure 2, as the latter shows stronger absolute enhancement than the high-field peak ($B = 0.390$ T). The protocol for hyperpolarization is represented in Figure 3c. It consists in repeating the cycle of consecutive laser pulse initialization and microwave driving, in order to gradually build up polarization for the ¹³C spins.

For improving the robustness properties of PulsePol, a possibility is to use the variant in Figure 3b from Tratzmiller *et al.*,⁴⁹ which relies on alternative pulse phase definitions compared to the original sequence in Figure 3a (hence the

label ‘phase-offset PulsePol’). Besides the increased robustness against frequency detuning, which could be verified by performing ¹³C hyperpolarization in single crystal diamond (SI, sect. S6.1), the phase-offset variant is also expected to mitigate inhomogeneities in the Rabi drive to a degree comparable to what is achieved in the standard PulsePol. The resonance condition for polarization transfer can be expressed similarly in both sequences as $\tau = \frac{n\pi}{\omega_I}$ where τ is the length of the 6-pulse block (Figure 3) and ω_I is the Larmor frequency of the target nuclear spins. However, the phase-offset PulsePol has half-integer resonances (see SI, sect. S6.2), contrasting with the odd-integer resonances $n = 1, 3, 5, 7$, etc. as in the original PulsePol. In the present scenario, in which the microwave excitation is resonant with NV which are at perpendicular orientation to the magnetic field, the choice of the resonance index n revealed to be non-trivial. Similarly to the case of the original PulsePol in Figure 3a, in which the $n = 3$ resonance is predicted to be optimal for polarization transfer,⁴⁰ the $n = 3.5$ condition was expected to offer better performance using the phase-offset PulsePol. However, our results suggest an improvement in the polarization transfer rate by using rather $n = 4.5$. This can be explained considering the dynamics involving the ¹⁴N nuclear spin of the NV, whose state can evolve during the application of the PulsePol sequence, owing to the presence of transitions that affect simultaneously the NV and ¹⁴N spin (which show finite probability as the transverse magnetic field breaks the defect C_{3v} symmetry). Simulations demonstrate that choosing the $n = 4.5$ resonance is in fact quasi-optimal for refocusing the NV-¹⁴N interaction and thereby avoiding inhibition of the polarization transfer to ¹³C by this dynamic (see SI, sect. S6.1 for comparison of the different resonances and the description of NV-¹⁴N interaction).

Although using the more robust sequence variant in Figure 3b provides a gain in the number of NV participating in the polarization transfer process, it is beneficial to implement strategies for increasing further the number of contributing NV. We now discuss such additional methods, optimize them by detecting the hyperpolarized signal in the 2 μ m sample, before applying them as well to the 100 nm nanodiamonds.

The first method consists in replacing the individual rectangular pulses by ‘‘composite’’ versions to provide further robustness to frequency detuning. We consider composite pulses described by Shaka *et al.*,⁵² which are built by adding ‘sidebands’ of alternating phases around a central rectangular pulse. In this work, the pulses by Shaka *et al.* are refined by the introduction of waiting times, and then numerically optimized, in order to improve their robustness. In our conditions $\Omega_1 = (2\pi)10.5$ MHz we determined that the simplest (two-sideband) version of the pulses leads to efficient operation of PulsePol in the range $\Delta_{\text{pol}} = (2\pi)15$ MHz (see SI, sect. S6.3 for description of the pulses optimization and sequence robustness properties). Owing to the asymmetric shape of the peak, the magnetic field was offset by a few gauss to maximize the number of addressed NV, as shown in inset of Figure 2, where we have represented a spectral region corresponding to the 15 MHz of excitation width. We estimate that this spectral region covers approximately a fraction of 4% of all centers, corresponding to NV oriented with a tilt (θ) from the magnetic field such that $|\theta - 90^\circ| \lesssim 2.5^\circ$ (see SI, sect. S8.1 and S8.2). In Figure 4c, the hyperpolarized ¹³C signals obtained using the standard and the optimized two-sideband pulse are compared, showing an improvement by about 30% compared to the latter (setting parameters such as the repetition number $M = 68$, and the sequence repetition time $\tau_{\text{SRT}} = 1.5$ ms, which appeared to be optimal, from SI, sect. S6.4). We note that the duration of the pulses is constrained by the chosen PulsePol resonance condition, as it is visible from Figure 3, the length of the π pulse should not exceed $\tau/4$. This restricted us from using ‘higher-order’ versions (i.e. with more than two sidebands) of the pulses, even though these are predicted to be more efficient. These would be within reach using a more powerful amplifier.

As an additional approach for enhancing the signal, we implemented slow sample rotation, around an axis perpendicular to the magnetic field (Figure 4a-b). This allows cycling through different NV subsets, as those defined by the excitation region of PulsePol will be progressively replaced, upon rotation, by NV of different initial orientation. The slow sample rotation implemented as in Figure 4b will bring, in fact, the axis of any NV to a direction orthogonal to the magnetic field, ensuring its spin transitions meet the 90° resonances. We rotate at speeds up to 25 °/s -the maximum allowed by our rotation stage- and obtain an increase in the ¹³C signal that is remarkably two-fold at the maximum velocity (Figure 4d). This suggests that switching regularly the subset of NV that is addressed by the polarization transfer sequence is favorable, compared to using continuously the same subset.

We can understand this observation, from the dynamics of the ¹³C polarization buildup. Without applying rotation, the increase of signal with the polarization time follows a so-called stretched exponential function $s(t) = A \left(1 - \exp \left\{ - \left(\frac{t}{T_{\text{pol}}} \right)^\beta \right\} \right)$, with $T_{\text{pol}} = 29(4)$ s and $\beta = 0.70(8)$ (SI, Figure S14). Consequently, efficient polarization occurs at short times, $s(t) \sim \left(\frac{t}{T_{\text{pol}}} \right)^\beta$, as $\beta < 1$. It was previously observed that:⁵³ 1) initially, the buildup occurs due to direct polarization of ¹³C spins from NV or spin diffusion on short length scales, while at longer times, it acquires (slower) dynamics impacted by the less efficient spin diffusion at longer scales, and 2) the NV acts in its very close surroundings, as a relaxation sink for nuclear spins shortening their T_1 . Here, we exploit this dynamic to benefit from the efficient polarization creation regime at short times (by rotating the sample) but still address distant ¹³C spins, with a long nuclear T_1 . From Figure 4d, increasing the rotation speed (ω_r) first enhances steeply the signal $s(\omega_r)$, which reaches an apparent saturation at high speeds. This behavior can be fitted as $s(\omega_r) = s_0 + a \left(1 - \exp \left\{ - (\omega_r / \omega_{r,0})^\beta \right\} \right)$,

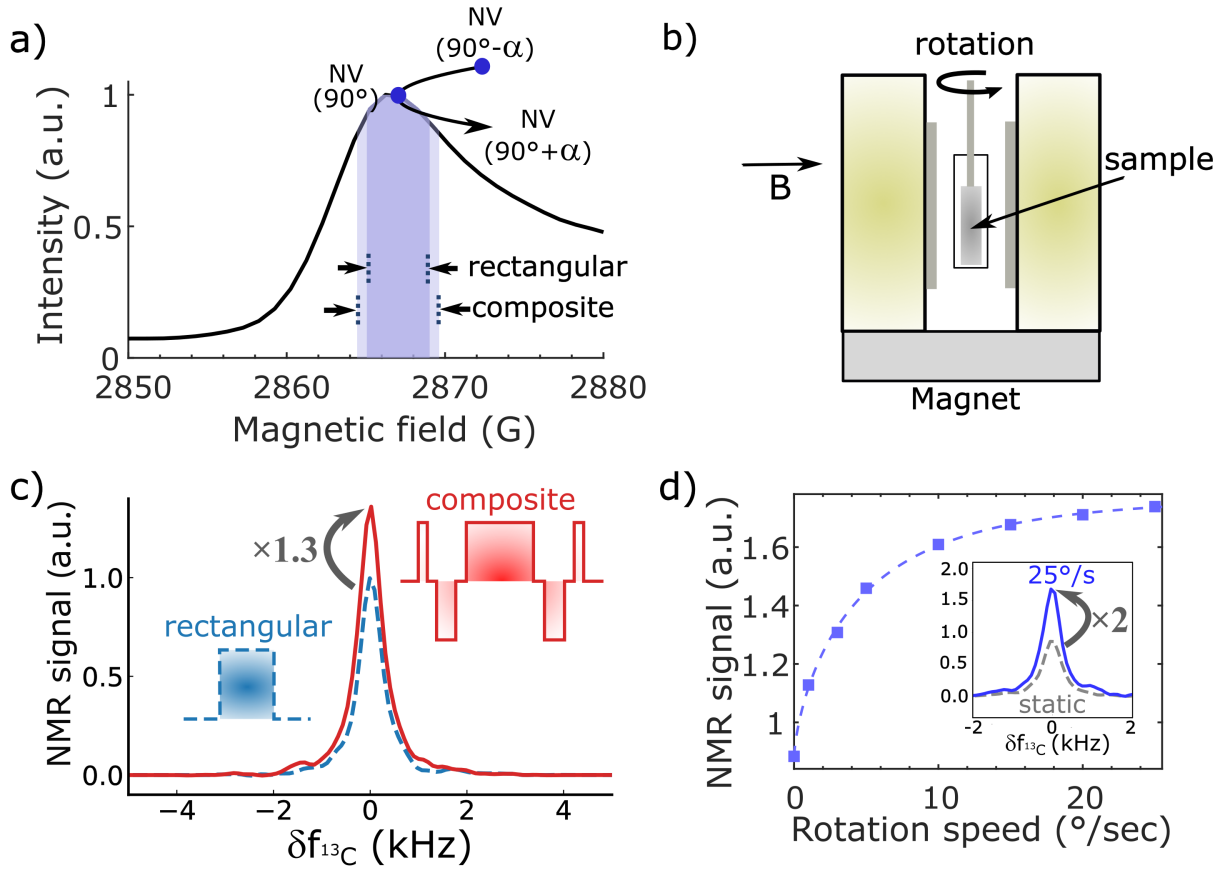


Figure 4: a) NV EPR spectral line with an illustration of strategies to increase the number of NV participating in polarization transfer. The microwave excitation bandwidth is extended by using composite pulses. Sample rotation enables a larger number of NV with various orientations to the magnetic field to pass through the microwave excitation region. b) Illustration showing the orientation of the rotation axis in the experimental setup c) Comparison of the hyperpolarized ¹³C NMR signals obtained using rectangular and composite pulses. d) Hyperpolarized ¹³C NMR signals obtained with sample rotation at different speeds. The dashed line is a stretched exponential fit as described in the text, yielding parameters $\omega_{r,0} = 4.9(5)^\circ/\text{s}$ and $\beta = 0.74(6)$ as the stretch exponent. Acquisitions represented on this figure were taken on the 2 μm sample.

that is a stretched exponential, from which $\omega_{r,0} = 4.9(5)^\circ/\text{s}$ is extracted and $\beta = 0.74(6)$. The stretched exponential behavior reminds of that of the polarization buildup. In fact, it is instructive to consider the overall rotation angle during the nuclear polarization buildup time $\omega_r T_{\text{pol}}$. At a speed $\omega_r \approx \omega_{r,0}$ one has $\omega_r T_{\text{pol}} = \omega_{r,0} T_{\text{pol}} = 142(20)^\circ$, which is close to the condition when *half a turn* (180°) is performed during T_{pol} . Thus, the significant signal increase provided by rotation in the range of speed $\omega_r < \omega_{r,0}$ occurs as more of the different NV subsets are progressively being involved in the polarization transfer, until all NV participate (at $\omega_r \approx \omega_{r,0}$). At the maximum speed ($25^\circ/\text{s}$), we measure a polarization buildup time $T_{\text{pol}} = 34(2)$ s comparable to that in the static sample. As the buildup dynamic is ultimately determined by the relaxation properties (T_1) of the spins that are being polarized, our observation indicates that ¹³C populations with comparable T_1 are being addressed, in the experiments with and without rotation. Since the signal is maximally increased by rotation ($25^\circ/\text{s}$), we use this setting in the rest of our experiments.

The ¹³C hyperpolarized signal that results from combining the above-mentioned strategies is represented in Figure 5. The corresponding enhancements over the ¹³C thermal signal ($\epsilon_{^{13}\text{C}}$) at the polarization field are $\epsilon_{^{13}\text{C}}^{2\mu\text{m}} = 1500$ and $\epsilon_{^{13}\text{C}}^{100\text{nm}} = 940$. To our knowledge, this is the first demonstration of hyperpolarization using an optically pumped color center at ambient conditions in diamond nanoparticles (< 200 nm). It is worthwhile to remark the speed at which the signal in Figure 5 is achieved, i.e. running the DNP protocol for 5 min, which is sufficient to reach the maximum of the buildup for both samples. We measured 34(2) s and 32(5) s as buildup times (T_{pol}) in the 2 μm and 100 nm particles, respectively. Relaxation times of 142(16) s and 116(16) s govern the decay of the hyperpolarized signal

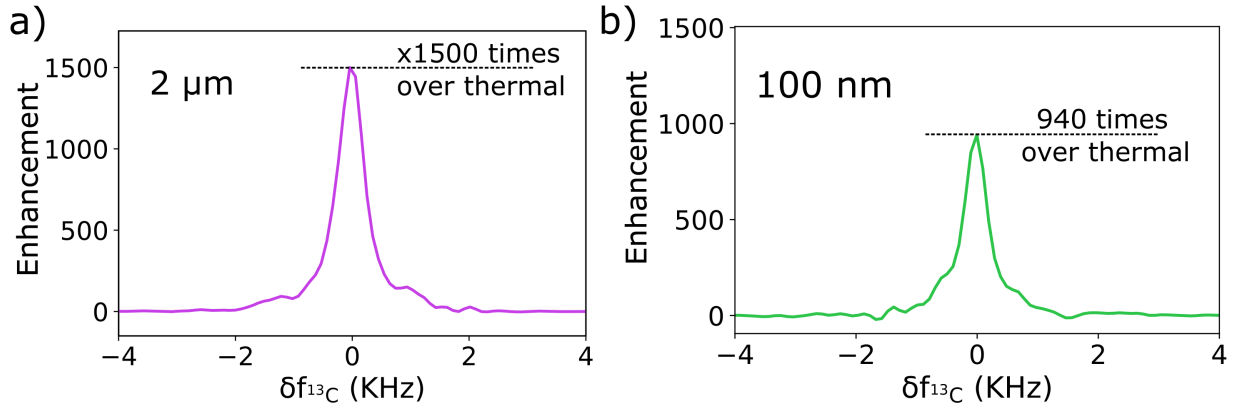


Figure 5: ¹³C NMR signal obtained after 5 min of hyperpolarization for a) 2 μm and b) 100 nm diamond particles. The spectra intensities are normalized by the ¹³C thermal signal at the polarization field (0.287 T), showing enhancements of 1500 and 940 times in a) and b), respectively.

Table 1: Summary of the sample properties. P1, NV concentrations and NV relaxation times are determined by X-band EPR. The T_2 time of NV is measured by Hahn echo ($\pi/2 - \pi$) in pulsed EPR and the T_1 time is obtained by fitting the decay of the echo-detected NV signal following a laser pulse. The ¹³C hyperpolarization is characterized by the buildup with the time T_{pol} , and the enhancement $\epsilon_{13\text{C}}$ (at the polarization field, $B = 0.287$ T), after combining all approaches for signal improvement described in the text.

Particle size	[P1]	[NV]	^{NV} T_2	^{NV} T_1	T_{pol}	enhanc. $\epsilon_{13\text{C}}$
2 μm	39(2) ppm	8.2(5) ppm	2.6(1) μs	3.82(4) ms	34(2) s	1500
100 nm	18(1) ppm	3.4(2) ppm	2.7(1) μs	4.23(7) ms	32(5) s	940

at 1 T magnetic field (SI, sect. S4). A significantly stronger enhancement is observed in the 2 μm sample. In the simplest description, for sample of similar polarization buildup times and neglecting effects of NV-NV interaction, we expect the enhancement factor to scale with the efficiency of NV initialization and their density, so that $\epsilon_{13\text{C}} \propto (\Delta\rho)_{\text{NV}} \cdot [\text{NV}]$. Thus, from the NV concentrations (Table 1), and from the determined $(\Delta\rho)_{\text{NV}}$, one would expect $\epsilon_{13\text{C}}^{2\mu\text{m}} / \epsilon_{13\text{C}}^{100\text{nm}} = \frac{0.024}{0.032} \cdot \frac{8.2\text{ ppm}}{3.4\text{ ppm}} = 1.8$, which is close to what we observe, i.e., $\frac{1500}{940} = 1.6$. To explain the small discrepancy between 1.8 and 1.6, we would like to point to a possible role of NV-NV interactions, which should result in faster NV decoherence in the case of dense NV ensembles during the application of PulsePol. Although this is outside of the scope of the present work, it might be beneficial, when working with extremely dense NV ensembles, to apply sequence modifications for refocussing the dipole-dipole interaction between the different NV.⁵⁴

Our findings allow discussing the spatial distribution of the polarized ¹³C spins, which is of fundamental interest. Considering the natural isotopic content (1.1%) of ¹³C in our samples, the spread of polarization by spin diffusion is predicted to follow the coefficient $D = 6.7 \times 10^{-15} \text{ cm s}^{-235}$. Taking into account our buildup times, $T_{\text{pol}} \sim 30$ s, we obtain as diffusion length $l \sim \sqrt{DT_{\text{pol}}} = 4$ nm. For randomly distributed defects, the nearest-neighbour distance is $r_{\text{NN}} = 0.55n^{-1/3}$, where n is defect density. We calculate that the NV concentrations in Table 1 correspond to comparable distances, $r_{\text{NN}} = 4.9$ nm and $r_{\text{NN}} = 6.5$ nm, for the 2 μm and 100 nm samples, respectively. In our samples, spin diffusion therefore leads the polarization to reach most parts of the diamond lattice between the different NV, which is in line with conclusions drawn previously in the context of single crystal experiments.⁵⁵

Although our efforts were focused on NV in the diamond material, our approach can be extended to centers with optical pumping capability in different host lattices. Spectral broadening induced by the anisotropy, that we observe for NV, will occur similarly for other known defects, such as pentacene in naphthalene crystals, or the divacancy in silicon carbide ($S = 1$). Our results highlight the interest of using the PulsePol sequence, that addresses all the centers in a given spectral range in parallel, while performing sample rotation to progressively bring into resonance centers that are initially unaddressed. Using PulsePol is also favorable for optimizing sequence timings, as illustrated by the small fraction of time it takes in the full polarization cycle. To obtain the signal in Figure 5, the sequence in Figure 3b was used with a duration $M\tau \approx 50 \mu\text{s}$ (for $M = 68$), which is much shorter than the laser initialization pulse (400 μs), the repetition interval ($\tau_{\text{SRT}} = 1.5$ ms) and the decay of NV polarization (${}^{\text{NV}}T_1 > \text{ms}$). There exists intervals, both between the pulses and after, where the PulsePol sequence could be applied at different carrier

frequencies. In future developments, this could be considered for improving our bandwidth (Δ_{pol}) and thus enhancing further the hyperpolarized signal (SI, sect. S7). Frequency sweeps, in contrast, typically address the centers slowly and sequentially, which can make the optimization of sequence timings more difficult and constrained.

Let us consider from the enhancement factors in Figure 5 the absolute nuclear polarization, defined as $p_{13\text{C}} = \frac{N_{\uparrow} - N_{\downarrow}}{N_{\uparrow} + N_{\downarrow}}$ where $N_{\uparrow}, N_{\downarrow}$ are the populations of the two Zeeman spin states of ¹³C. The value of $p_{13\text{C}}$ constitutes a figure of merit that is independent on the detection field. Applying the enhancement values observed in Figure 5 to the Boltzmann population, $p_{13\text{C,thermal}} \approx \frac{\hbar\omega_I}{2k_B T} = 2.52 \times 10^{-7}$ (room temperature, 0.287 T), we obtain 0.038% and 0.024% as $p_{13\text{C}}$ for the 2 μm and 100 nm powder samples, respectively. We discuss this outcome in the light of the work from King *et al.*,³³ who employed single crystal diamond with similar bulk material properties as our powders (electron-irradiated type Ib diamond). In that work, after performing DNP at 0.42 T magnetic field, the value of 6% of absolute ¹³C polarization was observed, which exceeds by a factor of 160 our best result (2 μm particles). We attribute this discrepancy to the combination of several factors as follows. First, King *et al.* performed NV-¹³C polarization transfer using NV aligned to the magnetic field in single crystal diamond, which represents the ideal conditions for generating high electron spin polarization by optical pumping. Although the precise enhancement of NV signal by illumination was not reported, it is common to reach, under such conditions, a population difference between the optically pumped ($m_S = 0$) and any of the optically depleted ($m_S = \pm 1$) states that obeys $(\Delta\rho)_{\text{NV}} > 30\%$,⁴⁵ i.e., improved more than 10-fold compared to our powders. We note that, besides the absence of light scattering, the suppression of spin state mixing for this NV alignment also likely plays a role in the improvement on $(\Delta\rho)_{\text{NV}}$ (which accounts for a factor of about two, according to the model fitting our powder spectrum, described in SI, sect. S3.2). Second, NV in single crystal belong to four homogeneously oriented subsets. This enables working conveniently with a fourth of all NV (25%), which yields in comparison to our powder another factor 25/4 (≈ 6). Thus, it is not surprising to observe > 60 increases in the enhancement factor in single crystal, compared to powder in the present conditions of our work.

From these considerations, one can suggest possible ways to increase the ¹³C enhancement further by adjusting some experimental parameters. We expect that combining the the application of the sequence at different frequencies (multiplexing) and pulse shaping would enable increasing the width of the spectral range Δ_{pol} to 100 MHz, which corresponds to about 16% of NV (SI, sect. S7). Better initialization of NV could be achieved through the use of higher laser intensities, however, in our experimental configuration, the laser intensity that can be applied was limited by sample heating. Temperature elevation in our micro- and nanodiamonds was estimated from resonance shift in the NV EPR spectrum, to be 51 K for the 2 μm particles and 24 K for the 100 nm particles (SI, section S3.3). We employed, for both samples, a configuration in which the diamond particles are densely packed, which favors localized heating. Better heat dissipation would be attained using an illumination geometry that allows also for the sample to be sparsely dispersed, in a gel or a liquid (possibly still using microstructured waveguides to counter light scattering). Although the realisation might present some challenges, this could be combined with some designs already employed for efficient cooling.⁵⁶

Dispersion in a fluid might promote particle reorientation by thermal motion, which in fact has been a proposed alternative to mechanically rotating the sample during the application of the polarization sequence.⁵⁰ However, the fluid viscosity, which determines the tumbling rate for nanodiamonds of a given size, might need to be carefully controlled as the reorientation dynamics should not make the nanodiamonds depart strongly from their orientation while NV are being driven by microwave. For a particle with $r = 80$ nm as hydrodynamic radius, using the Stokes-Einstein-Debye relation for the rotational diffusion coefficient, $D_r = k_B T / 8\pi\eta r^3$ in glycerol of dynamic viscosity $\eta = 1.4$ Pa s at room temperature ($T = 293$ K), one has $D_r = 0.22$ s⁻¹. In the conditions of our experiment, the region of efficient polarization transfer lies within a $90 \pm 2.5^\circ$ angle range from the magnetic field direction. Considering the RMS diffusion angle $\delta = \sqrt{2D_r t}$, thermal motion will drive the nanodiamond out of this orientation range after a time $t \approx 4.3$ ms. The ‘residence time’ is longer by two orders of magnitude than the duration of application of PulsePol in our protocol ($M\tau \approx 50$ μs), thus microwave driving with PulsePol will remain effective. The full polarization transfer cycle including initialization, microwave driving and waiting time, takes 1.5 ms and therefore could be applied 3 times, on average, before the nanodiamond moves to a less favorable orientation. This number of repetitions lies below what we established by mechanical rotation (> 130 polarization cycles, corresponding to > 200 ms), however, the viscosity of the fluid could be varied, e.g. by moderate cooling, to make the number of repetitions comparable. Our findings suggest indeed that *slow* reorientation, that ensures most nanodiamonds enter the bandwidth during the nuclear T_1 time, is already sufficient to provide a significant improvement in the hyperpolarized signal.

Turning to the polarization decay time ($^{13}\text{C}T_1$), it can be seen from the above-reported values that the decay in our samples occurs must faster than what has been reported for ultrapure single crystals,²¹ which we attribute to the high concentration of paramagnetic species (P1, NV and others), providing relaxation channels via flip-flops, or via their own T_1 process.⁵⁵ We now discuss consequences in terms of applications and possible routes for material development.

Despite being low by the standards of ultrapure diamond, the ¹³C T_1 times we observe are expected to be sufficient for some applications. A possible follow-up experiment to our work would consist in using “core-shell” particles, in which it is possible to obtain comparable T_1 times for a highly ($\sim 100\%$ ¹³C) isotopically enriched shell, overgrown on naturally abundant nanodiamonds containing NV, similar to the material used in the current work.⁵⁷ As originally reported, this would enable mediating spin polarization transferred from NV in the “core”, towards the surface, using spin diffusion in the enriched shell. This opens exciting perspectives of applications in which external substances could be hyperpolarized. This could apply to solids or very viscous liquids, as polarization transfer could be achieved by cross-polarization sequences. In conventional liquids, it could occur via the nuclear Overhauser effect, although the optimization of polarization transfer might require considering specific dynamics of the fluid at the surface of the nanoparticles.¹⁶ Besides, provided NV initialization and microwave driving can repeatedly be applied, such nanodiamonds would constitute a replenishable source of polarization. In particular, this could be of direct interest for NMR detected *in-situ*, as there, it is sufficient to have nuclear T_1 times of the order of one minute (or even slightly lower) both in the diamond nanoparticle and in the external substance.¹⁶

For another envisioned application, using nanodiamonds in MRI as tracers, it must be kept in mind that the ¹³C polarization must survive while the nanodiamonds diffuse to the location of interest (e.g., tumor) which can be long.⁵⁸ This points to a possible limitation of the material employed in the present study, for which the ¹³C T_1 restricts the time before detection to a few minutes. An approach for improving the nuclear T_1 consists in performing electron-irradiation on a sample with low nitrogen content, with the rationale of keeping the overall content of paramagnetic spins low. This was demonstrated to provide hour-long lifetimes in single crystals while still allowing efficient ¹³C hyperpolarization.³⁴ Recently, long coherence for NV under Hahn echo and dynamical decoupling were observed in milled chemical vapor deposition diamond, suggesting the possibility of producing ~ 200 nm particles with low magnetic noise levels, comparable to that in high-quality bulk material.⁵⁹ In smaller particles (100 nm and below), however, one might need to consider as well dangling bonds, or impurities in the diamond which are thought to be stabilized as a co-product of surface irregularities.^{29,60} The desired reduction in the number of the surface-related defects in particles of 100 nm and below might require the combination of material engineering for producing particles of near-spherical shape with a smooth surface, and approaches for reduction or passivation of possibly remaining defects.

Conclusion

Combining improvements on the material and in the dynamical nuclear polarization protocol, we demonstrated the hyperpolarization of ¹³C in diamond particles down to 100 nm size, using the optically pumped NV center as polarization source. In the nanoparticles, the impact of the magnetic noise from surface sources is reduced by combining treatments of air-oxidation and triacid cleaning, ensuring a long T_1 for the ¹³C spins. For improved NV initialization, the light scattering by the nanoparticles is mitigated by performing illumination using microstructured waveguides. To reduce the impact of the spectral broadening of NV in powder samples, the PulsePol sequence is optimized, and slow sample rotation (25 °/s) is performed. In contrast with protocols previously used for nanodiamonds (< 200 nm), our approach does not require cryogenic temperatures. The current results establish NV-containing nanodiamonds as a platform for hyperpolarization based on ¹³C spins at ambient conditions, promising future applications in the fields of sensitive nuclear magnetic resonance or MRI.

Experimental Section

Diamond powders with approximately 2 μm and 100 nm median particle size (Pureon AG, type Ib, HPHT, MSY1.5-2.5 and MSY 0-0.2) were used as starting material. To form NV, the samples were electron-irradiated with a dose of $3 \times 10^{18} \text{ cm}^{-2}$ in a 10 MeV electron accelerator operating under permanent argon flow. The temperature during the irradiation was maintained at 800 °C by controlling the dose per pulse and repetition frequency of the accelerator. To clean the surface of diamond particles from graphitic residues, the air oxidation (AO) treatment consists in annealing the samples at 620 °C for 5 hours in air.⁴¹ For removing metallic residues, the tri-acid cleaning (TAC) treatment consists in exposition to a high-concentration three-acid mixture of HNO₃(40%), HClO₄(70%), H₂SO₄(90%) in 1:1:1 proportions, under conditions of 200 °C temperature and 6 bar pressure, for approximately 2 hours. To prepare samples for the hyperpolarization experiment, a mass of 12 mg was used for the 2 μm powder. For the 100 nm sample, 6 mg was used.

The longitudinal relaxation times of ¹³C nuclear spins shown in Figure 1a were obtained using a 300MHz WB NMR system at room temperature and $B = 7.05 \text{ T}$ magnetic field, equipped with an Avance III console (Bruker Biospin GmbH).

Characterization of paramagnetic defect concentrations and their spin properties, as well as the implementation of polarization transfer from NV to ¹³C nuclear spins, were made with the X-band Bruker Elexsys E580 spectrometer (9-10 GHz). The ER-4122-SHQE resonator was used for spin-counting using continuous wave (CW) EPR. The pulsed FlexLine resonator ER-4118X-MD5 with the traveling wave tube (TWT) amplifier from Applied System Engineering, Inc. (Model no. 117) served to characterize the NV T_1 and T_2 times. Nuclear hyperpolarization was performed using the pulsed-ENDOR EN-4118X-MD4 resonator. To address the duty cycle limitations of the TWT amplifier, a 40 Watt CW solid-state microwave amplifier from AR Deutschland GmbH (40S6G18B 6-18 GHz) was employed, replacing the TWT. The sequences shown in Figure 3 were implemented with the Bruker SpinJet AWG. To perform *in situ* detection of the hyperpolarized ¹³C NMR signal, we used the RF coil of the ENDOR resonator. A tank circuit was added outside the resonator for tuning and matching, allowing for detection of NMR signal around the resonance frequency of ¹³C spins at 1 T ($\nu_{13\text{C}} \sim 10.7 \text{ MHz}$). The NMR signal is detected using a KEA² console (Magritek GmbH) using a 500W RF amplifier from (BT00500-ALPHA-SA from Tomco Technologies) for pulse amplification. To obtain the data represented in Figure 4 and 5, the hyperpolarized signal was accumulated 5 times. Acquisition of the ¹H NMR signal from a water sample of known volume was used as an intensity reference in order to determine the ¹³C signal enhancement values in Figure 5 (see SI, sect. S5, for details on the enhancement determination).

For illumination, a 3 W 532 nm Diode-Pumped Solid State (DPSS) laser from Laserglow Technologies was used and pulsed using TTL modulation. A 1.5 mm multimode fiber delivers light onto the waveguide structure as shown in SI, Figure S7. Due to losses, the power at the output of fiber is 1.6 W. The laser pulse length was set to 700 μs when measuring spectra as in Figure 2, and to 400 μs in the hyperpolarization experiment. Considering the repetition time of 1.5 ms, the 400 μs correspond to an average laser power of 420 mW. At this power, the illumination induces some heating of the samples, which was evaluated to be 51 K and 24 K for the 2 μm and 100 nm respectively (SI, section S3.3).

The X-ray photoelectron spectroscopy (XPS) acquisitions described in SI were performed using a Physical Electronics instrument (PHI 5800). The equipment was equipped with a hemispherical electron analyzer, a monochromatic Al $K\alpha$ X-ray source (1486.6 eV), and a flood gun to prevent sample charging. The spectra were recorded with a pass energy of 93.9 eV and 29.35 eV for the survey and the high-resolution spectrum, respectively. The XPS spectra were calibrated using the C1s peak as a reference, which corresponds to a binding energy of 284.7 eV.

Acknowledgements

We acknowledge Junichi Isoya for providing the single crystal diamond used for pre-testing the polarization sequences and Joachim Bansmann for assistance with XPS acquisition.

F. J. and M. B. P. acknowledge support via the ERC Synergy Grant HyperQ (Grant no. 856432) and the EU via the project QuMicro (Grant No. 01046911). F. J. acknowledges support from the EU via the project FLORIN (Grant no. 101086142), QUANTERA via the project “Microfluidics Quantum Diamond Sensor”, Carl Zeiss Foundation via IQST, the projects QPHOTON and Ultrasens-Vir, and the DFG. M. B. P. acknowledges support via the EU project SPINUS (Grant no. 101135699), the EU project C-QuENS (Grant no. 101135359) and the German Federal Ministry of Education and Research (BMBF) under the funding program quantum technologies - from basic research to market via the project QuE-MRT (FKZ: 13N16447) and via the project QSens: Quantensensoren für die biomedizinische Diagnostik (QMED) (Grant no. 03ZU1110FF).

Conflict of Interest

The authors have no conflict of interest to declare.

Author Contributions

R. B. and Y. M. conducted the experiments and analyzed the data. M. K. developed the composite pulses and performed numerical simulations of the robustness of PulsePol. R. B. conducted complementary sequence simulations (at specific NV orientations). A. M. performed the automation of the complete DNP experiment. F. G., S. N. and A. K. contributed to initial simulations of light scattering, and performed the design of the waveguide array structure, F. G. optimized the 3d-printing process. W. K. and C. L. performed the electron-irradiation and annealing and air-oxidation. C. J. provided the base material and information on the size distribution. R. B., Y. M. and M. K wrote the manuscript with input from all others. M. B. P., A. K. and F. J. conceived the study.

Data Availability

The data that support the findings of this study are available from the corresponding authors upon reasonable request.

References

- ¹ James Eills, Dmitry Budker, Silvia Cavagnero, Eduard Y. Chekmenev, Stuart J. Elliott, Sami Jannin, Anne Lesage, Jörg Matysik, Thomas Meersmann, Thomas Prisner, Jeffrey A. Reimer, Hanming Yang, and Igor V. Koptuyug. Spin hyperpolarization in modern magnetic resonance. *Chemical Reviews*, 123(4):1417–1551, January 2023.
- ² Panayiotis Nikolaou, Boyd M. Goodson, and Eduard Y. Chekmenev. Nmr hyperpolarization techniques for biomedicine. *Chemistry – A European Journal*, 21(8):3156–3166, December 2014.
- ³ Zhen J. Wang, Michael A. Ohliger, Peder E. Z. Larson, Jeremy W. Gordon, Robert A. Bok, James Slater, Javier E. Villanueva-Meyer, Christopher P. Hess, John Kurhanewicz, and Daniel B. Vigneron. Hyperpolarized ¹³C MRI: State of the Art and Future Directions. *Radiology*, 291(2):273–284, May 2019.
- ⁴ Victor Ribay, Clément Praud, Marine P.M. Letertre, Jean-Nicolas Dumez, and Patrick Giraudeau. Hyperpolarized nmr metabolomics. *Current Opinion in Chemical Biology*, 74:102307, June 2023.
- ⁵ Yaewon Kim and Christian Hilty. *Applications of Dissolution-DNP for NMR Screening*, chapter 15, pages 501–526. Elsevier, 2019.
- ⁶ Andrea Bertarello, Pierrick Berruyer, Markus Artelsmair, Charles S. Elmore, Sepideh Heydarkhan-Hagvall, Markus Schade, Elisabetta Chiarparin, Staffan Schantz, and Lyndon Emsley. In-cell quantification of drugs by magic-angle spinning dynamic nuclear polarization nmr. *Journal of the American Chemical Society*, 144(15):6734–6741, April 2022.
- ⁷ Aude Sadet, Cristina Stavarache, Mihaela Bacalum, Mihai Radu, Geoffrey Bodenhausen, Dennis Kurzbach, and Paul R. Vasos. Hyperpolarized water enhances two-dimensional proton nmr correlations: A new approach for molecular interactions. *Journal of the American Chemical Society*, 141(32):12448–12452, August 2019.
- ⁸ Andrew G.M. Rankin, Julien Trébosc, Frédérique Pourpoint, Jean-Paul Amoureux, and Olivier Lafon. Recent developments in mas dnp-nmr of materials. *Solid State Nuclear Magnetic Resonance*, 101:116–143, September 2019.
- ⁹ Shira Haber and Michal Leskes. Dynamic nuclear polarization in battery materials. *Solid State Nuclear Magnetic Resonance*, 117:101763, February 2022.
- ¹⁰ Jan H. Ardenkjær-Larsen, Björn Fridlund, Andreas Gram, Georg Hansson, Lennart Hansson, Mathilde H. Lerche, Rolf Servin, Mikkel Thaning, and Klaes Golman. Increase in signal-to-noise ratio of ζ 10,000 times in liquid-state NMR. *Proceedings of the National Academy of Sciences*, 100(18):10158–10163, aug 2003.
- ¹¹ S. J. Nelson, J. Kurhanewicz, D. B. Vigneron, P. E. Z. Larson, A. L. Harzstark, M. Ferrone, M. van Criekinge, J. W. Chang, R. Bok, I. Park, G. Reed, L. Carvajal, E. J. Small, P. Munster, V. K. Weinberg, J. H. Ardenkjaer-Larsen, A. P. Chen, R. E. Hurd, L.-I. Odegardstuen, F. J. Robb, J. Tropp, and J. A. Murray. Metabolic Imaging of Patients with Prostate Cancer Using Hyperpolarized [1-¹³C]Pyruvate. *Science Translational Medicine*, 5(198):198ra108–198ra108, aug 2013.
- ¹² A. Henstra, T.-S. Lin, J. Schmidt, and W. Th. Wenckebach. High dynamic nuclear polarization at room temperature. *Chemical Physics Letters*, 165(1):6 – 10, 1990.

- ¹³ Makoto Negoro, Akinori Kagawa, Kenichiro Tateishi, Yoshiki Tanaka, Tomohiro Yuasa, Keigo Takahashi, and Masahiro Kitagawa. Dissolution dynamic nuclear polarization at room temperature using photoexcited triplet electrons. *The Journal of Physical Chemistry A*, 122(17):4294–4297, April 2018.
- ¹⁴ Tomoyuki Hamachi, Koki Nishimura, Hironori Kouno, Yusuke Kawashima, Kenichiro Tateishi, Tomohiro Uesaka, Nobuo Kimizuka, and Nobuhiro Yanai. Porphyrins as Versatile, Aggregation-Tolerant, and Biocompatible Polarizing Agents for Triplet Dynamic Nuclear Polarization of Biomolecules. *The Journal of Physical Chemistry Letters*, 12(10):2645–2650, March 2021.
- ¹⁵ Tim R. Eichhorn, Anna J. Parker, Felix Josten, Christoph Müller, Jochen Scheuer, Jakob M. Steiner, Martin Gierse, Jonas Handwerker, Michael Keim, Sebastian Lucas, Mohammad Usman Qureshi, Alastair Marshall, Alon Salhov, Yifan Quan, Jan Binder, Kay D. Jahnke, Philipp Neumann, Stephan Knecht, John W. Blanchard, Martin B. Plenio, Fedor Jelezko, Lyndon Emsley, Christophoros C. Vassiliou, Patrick Hautle, and Ilai Schwartz. Hyperpolarized Solution-State NMR Spectroscopy with Optically Polarized Crystals. *Journal of the American Chemical Society*, 144(6):2511–2519, February 2022.
- ¹⁶ Naoto Matsumoto, Koki Nishimura, Nobuo Kimizuka, Yusuke Nishiyama, Kenichiro Tateishi, Tomohiro Uesaka, and Nobuhiro Yanai. Proton hyperpolarization relay from nanocrystals to liquid water. *Journal of the American Chemical Society*, 144(39):18023–18029, 2022. PMID: 36109169.
- ¹⁷ Frank Alexis, Eric Pridgen, Linda K. Molnar, and Omid C. Farokhzad. Factors Affecting the Clearance and Biodistribution of Polymeric Nanoparticles. *Molecular Pharmaceutics*, 5(4):505–515, August 2008.
- ¹⁸ Grzegorz Kwiatkowski, Fabian Jähnig, Jonas Steinhauser, Patrick Wespi, Matthias Ernst, and Sebastian Kozerke. Direct hyperpolarization of micro- and nanodiamonds for bioimaging applications – Considerations on particle size, functionalization and polarization loss. *Journal of Magnetic Resonance*, 286:42–51, jan 2018.
- ¹⁹ David E. J. Waddington, Thomas Boele, Ewa Rej, Dane R. McCamey, Nicholas J. C. King, Torsten Gaebel, and David J. Reilly. Phase-Encoded Hyperpolarized Nanodiamond for Magnetic Resonance Imaging. *Scientific Reports*, 9(1):5950, April 2019.
- ²⁰ Grzegorz Kwiatkowski, Fabian Jähnig, Jonas Steinhauser, Patrick Wespi, Matthias Ernst, and Sebastian Kozerke. Nanometer size silicon particles for hyperpolarized MRI. *Scientific Reports*, 7(1), August 2017.
- ²¹ E. C. Reynhardt and G. L. High. Nuclear magnetic resonance studies of diamond. *Progress in Nuclear Magnetic Resonance Spectroscopy*, 38(1):37–81, January 2001.
- ²² Kai-Hung Yang and Roger J. Narayan. Biocompatibility and functionalization of diamond for neural applications. *Current Opinion in Biomedical Engineering*, 10:60–68, June 2019.
- ²³ Vadym N. Mochalin, Olga Shenderova, Dean Ho, and Yury Gogotsi. The properties and applications of nanodiamonds. *Nature Nanotechnology*, 7(1):11–23, December 2011.
- ²⁴ J. H. N. Loubser and J. A. van Wyk. Electron spin resonance in the study of diamond. *Reports on Progress in Physics*, 41(8):1201–1248, aug 1978.
- ²⁵ E. C. Reynhardt and G. L. High. Dynamic nuclear polarization of diamond. I. Solid state and thermal mixing effects. *The Journal of Chemical Physics*, 109(10):4090–4099, 1998.
- ²⁶ Christian O. Bretschneider, Ümit Akbey, Fabien Aussenac, Greg L. Olsen, Akiva Feintuch, Hartmut Oschkinat, and Lucio Frydman. On The Potential of Dynamic Nuclear Polarization Enhanced Diamonds in Solid-State and Dissolution ¹³C NMR Spectroscopy. *Chem. Phys. Chem.*, 17(17):2691–2701, 2016.
- ²⁷ Daphna Shimon, Kelly A. Cantwell, Linta Joseph, Ethan Q. Williams, Zaili Peng, Susumu Takahashi, and Chandrasekhar Ramanathan. Large Room Temperature Bulk DNP of ¹³C via P1 Centers in Diamond. *The Journal of Physical Chemistry C*, 126(41):17777–17787, oct 2022.
- ²⁸ B. V. Yavkin, G. V. Mamin, M. R. Gafurov, and S. B. Orlinskii. Size-dependent concentration of N0 paramagnetic centres in HPHT nanodiamonds. *Magn. Reson. Solids*, 17:15101, 2015.
- ²⁹ Z. Peng, T. Biktairov, F. H. Cho, U. Gerstmann, and S. Takahashi. Investigation of near-surface defects of nanodiamonds by high-frequency EPR and DFT calculation. *The Journal of Chemical Physics*, 150(13):134702, apr 2019.
- ³⁰ Dongyoung Yoon, Murari Soundararajan, Serguei Sekatski, Jérémy Genoud, Stefano Alberti, and Jean-Philippe Ansermet. High-Field ¹³C Dynamic Nuclear Polarization in Nanodiamond. *The Journal of Physical Chemistry C*, 123(34):21237–21243, 2019.
- ³¹ T. Boele, D. E. J. Waddington, T. Gaebel, E. Rej, A. Hasija, L. J. Brown, D. R. McCamey, and D. J. Reilly. Tailored nanodiamonds for hyperpolarized C13 MRI. *Physical Review B*, 101(15), apr 2020.

- ³² J Scheuer, J-M Cai, I Schwarz, A Retzker, M Katagiri, T Teraji, S Koizumi, J Isoya, et al. Detecting and polarizing nuclear spins with double resonance on a single electron spin. *Physical review letters*, 111(6):067601, 2013.
- ³³ Jonathan P. King, Keunhong Jeong, Christophoros C. Vassiliou, Chang S. Shin, Ralph H. Page, Claudia E. Avalos, Hai-Jing Wang, and Alexander Pines. Room-temperature in situ nuclear spin hyperpolarization from optically pumped nitrogen vacancy centres in diamond. *Nature Communications*, 6(1), dec 2015.
- ³⁴ J. Scheuer, I. Schwartz, Q. Chen, D. Schulze-Sünninghausen, P. Carl, P. Höfer, A. Retzker, H. Sumiya, J. Isoya, B. Luy, M. B. Plenio, B. Naydenov, and F. Jelezko. Optically induced dynamic nuclear spin polarisation in diamond. *New Journal of Physics*, 18(1):013040, January 2016.
- ³⁵ Anna J. Parker, Keunhong Jeong, Claudia E. Avalos, Birgit J. M. Hausmann, Christophoros C. Vassiliou, Alexander Pines, and Jonathan P. King. Optically pumped dynamic nuclear hyperpolarization in ¹³C-enriched diamond. *Phys. Rev. B*, 100:041203, Jul 2019.
- ³⁶ Ashok Ajoy, Kristina Liu, Raffi Nazaryan, Xudong Lv, Pablo R. Zangara, Benjamin Safvati, Guoqing Wang, Daniel Arnold, Grace Li, Arthur Lin, Priyanka Raghavan, Emanuel Druga, Siddharth Dhomkar, Daniela Pagliero, Jeffrey A. Reimer, Dieter Suter, Carlos A. Meriles, and Alexander Pines. Orientation-independent room temperature optical ¹³C hyperpolarization in powdered diamond. *Science Advances*, 4(5), 2018.
- ³⁷ Koichiro Miyanishi, Takuya F. Segawa, Kazuyuki Takeda, Izuru Ohki, Shinobu Onoda, Takeshi Ohshima, Hiroshi Abe, Hideaki Takashima, Shigeki Takeuchi, Alexander I. Shames, Kohki Morita, Yu Wang, Frederick T.-K. So, Daiki Terada, Ryuji Igarashi, Akinori Kagawa, Masahiro Kitagawa, Norikazu Mizuochi, Masahiro Shirakawa, and Makoto Negoro. Room temperature hyperpolarization of polycrystalline samples with optically polarized triplet electrons: Pentacene or Nitrogen-Vacancy center in diamond? *MR*, dec 2020.
- ³⁸ Max Gierrth, Valentin Krespach, Alexander I. Shames, Priyanka Raghavan, Emanuel Druga, Nicholas Nunn, Marco Torelli, Ruhee Nirodi, Susan Le, Richard Zhao, Alessandra Aguilar, Xudong Lv, Mengze Shen, Carlos A. Meriles, Jeffrey A. Reimer, Alexander Zaitsev, Alexander Pines, Olga Shenderova, and Ashok Ajoy. Enhanced Optical ¹³C Hyperpolarization in Diamond Treated by High-Temperature Rapid Thermal Annealing. *Advanced Quantum Technologies*, 3(10):2000050, sep 2020.
- ³⁹ G. Waldherr, J. Beck, M. Steiner, P. Neumann, A. Gali, Th. Frauenheim, F. Jelezko, and J. Wrachtrup. Dark States of Single Nitrogen-Vacancy Centers in Diamond Unraveled by Single Shot NMR. *Physical Review Letters*, 106(15), apr 2011.
- ⁴⁰ Ilai Schwartz, Jochen Scheuer, Benedikt Tratzmiller, Samuel Müller, Qiong Chen, Ish Dhand, Zhen-Yu Wang, Christoph Müller, Boris Naydenov, Fedor Jelezko, and Martin B. Plenio. Robust optical polarization of nuclear spin baths using Hamiltonian engineering of nitrogen-vacancy center quantum dynamics. *Science Advances*, 4(8), 2018.
- ⁴¹ Yuliya Mindarava, Rémi Blinder, Christian Laube, Wolfgang Knolle, Bernd Abel, Christian Jentgens, Junichi Isoya, Jochen Scheuer, Johannes Lang, Ilai Schwartz, Boris Naydenov, and Fedor Jelezko. Efficient conversion of nitrogen to nitrogen-vacancy centers in diamond particles with high-temperature electron irradiation. *Carbon*, 170:182–190, dec 2020.
- ⁴² Ch. Laube, Y. M. Riyad, A. Lotnyk, F. P. Lohmann, C. Kranert, R. Hermann, W. Knolle, Th. Oeckinghaus, R. Reuter, A. Denisenko, A. Kahnt, and B. Abel. Defined functionality and increased luminescence of nanodiamonds for sensing and diagnostic applications by targeted high temperature reactions and electron beam irradiation. *Materials Chemistry Frontiers*, 1(12):2527–2540, 2017.
- ⁴³ A. M. Panich, N. A. Sergeev, A. I. Shames, V. Y. Osipov, J.-P. Boudou, and S. D. Goren. Size dependence of ¹³C nuclear spin-lattice relaxation in micro-and nanodiamonds. *Journal of Physics: Condensed Matter*, 27(7):072203, 2015.
- ⁴⁴ T. Rosskopf, A. Dussaux, K. Ohashi, M. Loretz, R. Schirhagl, H. Watanabe, S. Shikata, K. M. Itoh, and C. L. Degen. Investigation of surface magnetic noise by shallow spins in diamond. *Phys. Rev. Lett.*, 112:147602, Apr 2014.
- ⁴⁵ M. Drake, E. Scott, and J. A. Reimer. Influence of magnetic field alignment and defect concentration on nitrogen-vacancy polarization in diamond. *New Journal of Physics*, 18(1):013011, dec 2015.
- ⁴⁶ Yuliya Mindarava, Rémi Blinder, Yan Liu, Jochen Scheuer, Johannes Lang, Viatcheslav Agafonov, Valery A. Davydov, Christian Laube, Wolfgang Knolle, Bernd Abel, Boris Naydenov, and Fedor Jelezko. Synthesis and coherent properties of ¹³C-enriched sub-micron diamond particles with nitrogen vacancy color centers. *Carbon*, 165:395–403, sep 2020.
- ⁴⁷ G. E. Pake. Nuclear Resonance Absorption in Hydrated Crystals: Fine Structure of the Proton Line. *J. of Chem. Phys.*, 16(4):327–336, 1948.

- ⁴⁸ Boris Yavkin, Marat Gafurov, Mikhail Volodin, Georgy Mamin, and Sergei B. Orlinskii. EPR and double resonances in study of diamonds and nanodiamonds. In *Experimental Methods in the Physical Sciences*, pages 83–113. Elsevier, 2019.
- ⁴⁹ Benedikt Tratzmiller, Jan F. Haase, Zhenyu Wang, and Martin B. Plenio. Parallel selective nuclear-spin addressing for fast high-fidelity quantum gates. *Physical Review A*, 103(1), jan 2021.
- ⁵⁰ Q. Chen, I. Schwarz, F. Jelezko, A. Retzker, and M. B. Plenio. Optical hyperpolarization of ¹³C nuclear spins in nanodiamond ensembles. *Phys. Rev. B*, 92:184420, Nov 2015.
- ⁵¹ Jochen Scheuer, Ilai Schwartz, Samuel Müller, Qiong Chen, Ish Dhand, Martin B. Plenio, Boris Naydenov, and Fedor Jelezko. Robust techniques for polarization and detection of nuclear spin ensembles. *Phys. Rev. B*, 96:174436, Nov 2017.
- ⁵² A.J Shaka and A Pines. Symmetric phase-alternating composite pulses. *Journal of Magnetic Resonance (1969)*, 71(3):495–503, 1987.
- ⁵³ William Beatrez, Arjun Pillai, Otto Janes, Dieter Suter, and Ashok Ajoy. Electron Induced Nanoscale Nuclear Spin Relaxation Probed by Hyperpolarization Injection. *Physical Review Letters*, 131(1), July 2023.
- ⁵⁴ Benedikt Tratzmiller. *Pulsed control methods with applications to nuclear hyperpolarization and nanoscale NMR*. PhD thesis, Universität Ulm, 2021.
- ⁵⁵ A. Ajoy, B. Safvati, R. Nazaryan, J. T. Oon, B. Han, P. Raghavan, R. Nirodi, A. Aguilar, K. Liu, X. Cai, X. Lv, E. Druga, C. Ramanathan, J. A. Reimer, C. A. Meriles, D. Suter, and A. Pines. Hyperpolarized relaxometry based nuclear T1 noise spectroscopy in diamond. *Nature Communications*, 10(1), nov 2019.
- ⁵⁶ Adrishia Sarkar, Brian Blankenship, Emanuel Druga, Arjun Pillai, Ruhee Nirodi, Siddharth Singh, Alexander Oddo, Paul Reshetikhin, and Ashok Ajoy. Rapidly enhanced spin-polarization injection in an optically pumped spin ratchet. *Phys. Rev. Appl.*, 18:034079, Sep 2022.
- ⁵⁷ Yuliya Mindarava, Rémi Blinder, Valery A. Davydov, Mustapha Zaghrioui, Viatcheslav N. Agafonov, Cécile Autret, Priyadharshini Balasubramanian, Raúl Gonzalez Brouwer, and Fedor Jelezko. “Core–Shell” Diamond Nanoparticles with NV– Centers and a Highly Isotopically Enriched ¹³C Shell as a Promising Hyperpolarization Agent. *The Journal of Physical Chemistry C*, 125(50):27647–27653, December 2021.
- ⁵⁸ Gordon Winter, Nina Eberhardt, Jessica Löffler, Marco Raabe, Md. Noor A. Alam, Li Hao, Alireza Abaei, Hendrik Herrmann, Claudia Kuntner, Gerhard Glatting, Christoph Solbach, Fedor Jelezko, Tanja Weil, Ambros J. Beer, and Volker Rasche. Preclinical PET and MR Evaluation of ⁸⁹Zr- and ⁶⁸Ga-Labeled Nanodiamonds in Mice over Different Time Scales. *Nanomaterials*, 2022.
- ⁵⁹ B. D. Wood, G. A. Stimpson, J. E. March, Y. N. D. Lekhai, C. J. Stephen, B. L. Green, A. C. Frangeskou, L. Ginés, S. Mandal, O. A. Williams, and G. W. Morley. Long spin coherence times of nitrogen vacancy centers in milled nanodiamonds. *Phys. Rev. B*, 105:205401, May 2022.
- ⁶⁰ Jyh-Pin Chou, Péter Udvarhelyi, Nathalie P. de Leon, and Adam Gali. *Ab Initio* study of (100) diamond surface spins. *Physical Review Applied*, 20(1), July 2023.

Supporting Information

to: ^{13}C Hyperpolarization with Nitrogen-Vacancy Centers in Micro- and Nanodiamonds for Sensitive Magnetic Resonance Applications

Contents

S1 Material	2
S2 Surface treatment characterization	3
S2.1 Monitoring surface spin defects by EPR	3
S2.2 ^{13}C T_1 relaxation	6
S2.3 NV T_1 relaxation	7
S2.4 XPS on smaller nanoparticles (~ 25 nm)	7
S3 Sample illumination	8
S3.1 Illumination protocol	8
S3.2 Phenomenological description of the NV spectrum in X-band EPR under optical pumping	10
S3.2.1 Redistribution of state populations	10
S3.2.2 Spectral fits	11
S3.3 Heating induced by illumination	14
S3.4 Transient NV signal under pulsed illumination	15
S4 Build-up and decay of ^{13}C polarization	16
S4.1 $2\ \mu\text{m}$ and $100\ \text{nm}$ samples, with sample rotation ($25^\circ/\text{s}$)	16
S4.2 Buildup for the $2\ \mu\text{m}$ sample, without rotation	17
S5 Evaluation of the hyperpolarization enhancement factor and the absolute polarization	17
S6 PulsePol parameter tuning	19
S6.1 Testing the robustness to detuning of the phase-offset PulsePol sequence . .	19
S6.2 Comparison of resonance indices $n = 3.5$ and $n = 4.5$	21
S6.3 The composite pulses	24
S6.4 Other parameters adjustment	27

S7 Potential adaptations for further increase of the bandwidth Δ_{pol}	27
S8 NV spin Hamiltonian	28
S8.1 Spin Hamiltonian diagonalization for NV centers under transverse B -field .	28
S8.2 Fraction of NV centers in the bandwidth Δ_{pol} ($\approx 90^\circ$ to the magnetic field)	30
S8.3 NV transition dipole and Rabi inhomogeneity	31
S8.4 NV transition frequencies in diamond powder at different magnetic fields . .	32

S1 Material

The commercial samples are Pureon AG, type Ib, HPHT, MSY1.5-2.5 and Pureon AG, type Ib, HPHT, MSY0-0.2 having about 2 μm and 100 nm median size, respectively. Scanning electron microscopy images are shown in Fig. S1. The size distribution parameters for the batches employed in this work are given in Table 1.

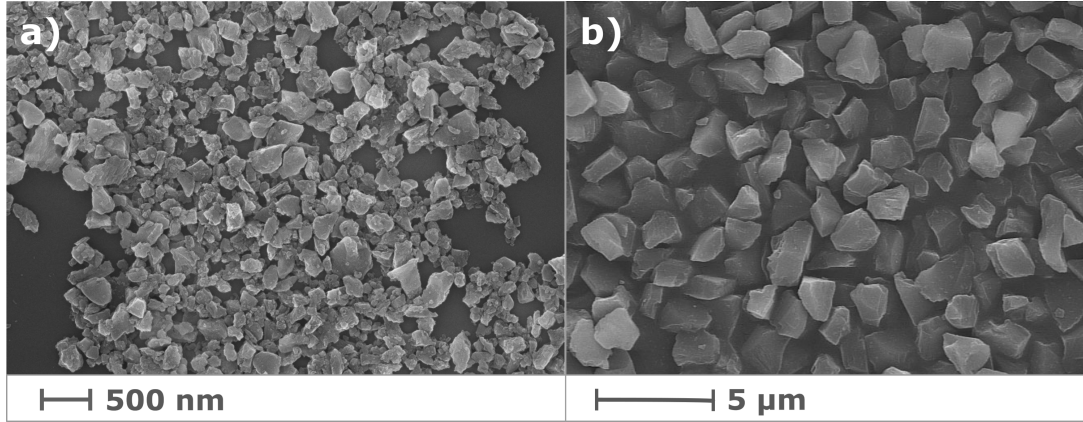


Fig. S1: Scanning electron microscopy images of a) 100 nm and b) 2 μm diamond powders, respectively Pureon AG, MSY0-0.2 and MSY1.5-2.5.

sample	median size (μm)	standard deviation (μm)
Pureon AG, MSY1.5-2.5, type Ib	1.95	0.31
Pureon AG, MSY0-0.2, type Ib	0.115	0.028

Table 1: Size distribution properties for the batches of diamond powder samples used in the present work.

S2 Surface treatment characterization

S2.1 Monitoring surface spin defects by EPR

EPR spectra were measured on the commercial 100 nm sample (Pureon AG MSY0-0.2 Type Ib, labelled ‘base material’) and after the several surface treatment steps summarized in Fig. S2.

In this study, the starting material is the commercial sample, with no NV centers formed by irradiation and annealing. To characterize the surface treatments, it is useful to perform two types of EPR measurements:

- A narrow scan around $g = 2$ (in a ~ 100 G range) at low microwave power. This allows resolving bulk and subsurface impurities [1], as well as dangling bonds with long relaxation times (e.g. in graphite). The corresponding acquisitions are shown in Fig. S3.
- An acquisition in a wide spectral range (6000 G), at higher microwave power, in order to resolve impurities with a broad spectra and short lifetimes. The spectra are shown in Fig. S4.

It is possible to observe the disappearance of a $g \sim 2$ contribution following the air-oxidation (AO) treatment (Fig. S3a). We attribute this effect to the removal of dangling bonds in graphite covering the nanodiamonds. This is associated with a strong change in color of the nanoparticles, initially black, which turn bright. in the color of the nanoparticles, which are initially black and become bright after the treatment.

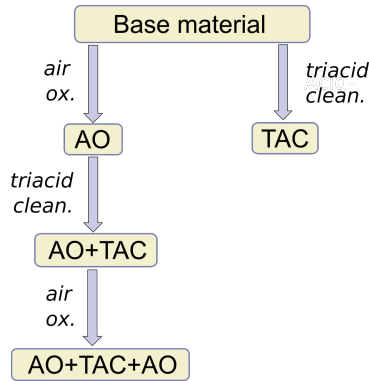


Fig. S2: Description of the surface treatment steps for the 100 nm sample.

The wide-range, high-power spectrum in Fig. S4. reveals also the presence of several broad contributions in the base material (covering a ~ 3000 G range). Although one contribution (labelled (1) in Fig. S4) is removed both by the AO and TAC treatments, another important contribution (labelled (2) in Fig. S4) persists after air-oxidation, but is removed

by the triacid (TAC) treatment. Iron constitutes a likely contaminant, as it is present in the beads used in the manufacturing process, for milling the material down to the desired particle size. In smaller nanodiamonds from the same manufacturer that underwent the AO treatment, the presence of iron is confirmed by XPS (sect. S2.4). Consequently: 1) we attribute the broad EPR contribution that is removed by the triacid cleaning, to iron-related spin impurities 2) we hypothesize that the fast fluctuations of these paramagnetic impurities explain the shortening effect on the T_1 of ^{13}C and NV (detailed in sections S2.2 and S2.3, respectively).

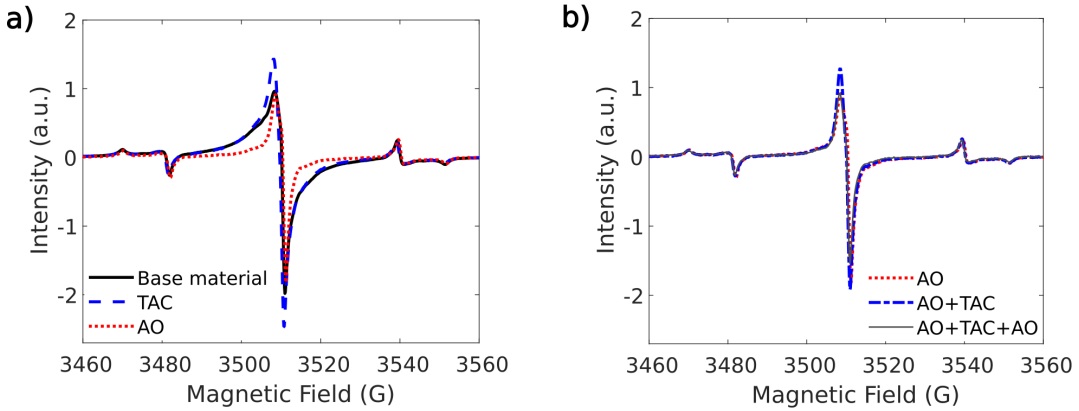


Fig. S3: CW EPR spectra in a narrow spectral range (100 G) around the $g = 2$ resonance, at low microwave power ($P_{\text{MW}} = 0.150 \mu\text{W}$). The acquisition frequency is $\nu = 9.84 \text{ GHz}$. The spectra are normalized to the sample mass and Q -factor. a) Spectra showing the effect of the first treatment steps (AO or TAC). The satellites at 3480 G and 3540 G correspond to the hyperfine lines of P1 centers. These satellites are unaffected by surface treatments, as expected for bulk impurities. The signal in the center comprises both the P1 central line, and $g \sim 2$ paramagnetic species. Although a minor change is observed with the triacid (TAC), a strong modification is observed following air-oxidation (AO), as the latter leads to the disappearance of one central component that we attribute to the efficient removal of graphite and associated dangling bonds. b) Effect of the successive treatment combinations. A small change in the intensity of the central line after the AO+TAC step, however, the spectrum remains essentially unaffected.

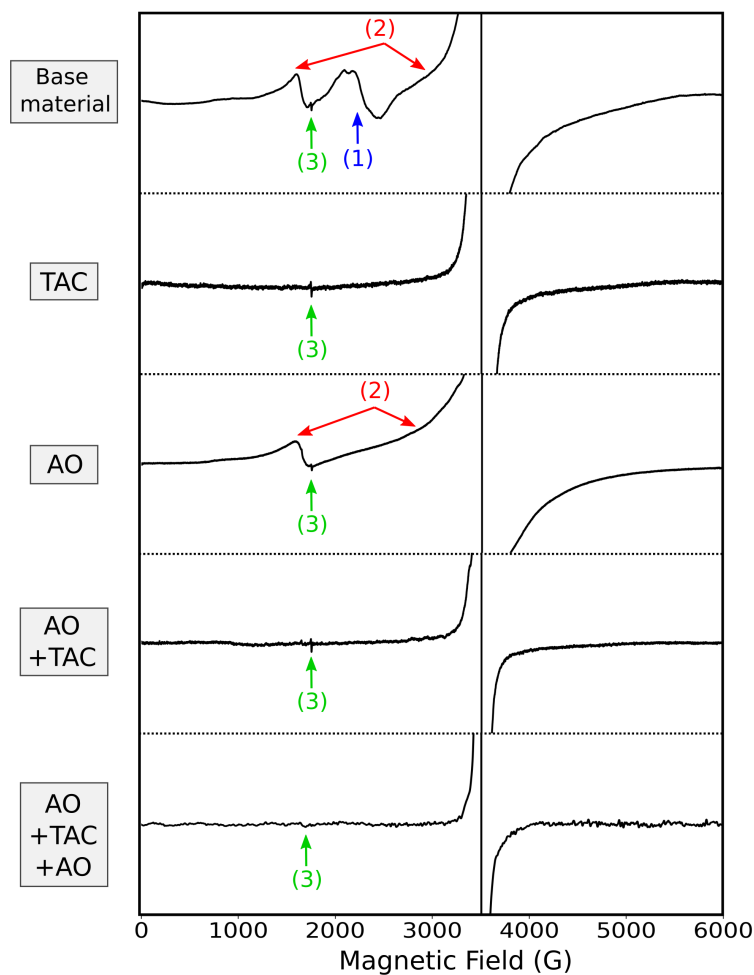


Fig. S4: CW EPR spectra in a broad spectral range (0-6000 G), at high microwave power ($P_{\text{MW}} = 23.7 \text{ mW}$). The acquisition frequency is $\nu = 9.84 \text{ GHz}$ and the data is normalized to the sample mass and Q -factor. The spectra are also trimmed vertically in order to better visualize, specifically, the broad contributions. The first spectrum shows an impurity contribution (1) removed both by the AO and TAC treatment. Another contribution, labelled (2), is removed by the TAC step only, and is associated to paramagnetic species of iron (see text). The contribution (3), which appears in the half-field region (at $g \sim 4$), might be associated with impurities of $S > 1/2$ multiplicity within the nanodiamonds. After the last treatment step (AO+TAC+AO), the contribution (3) is likely still present, but not observed due to longer spectrum averaging and possible magnetic field or frequency drifts.

S2.2 ^{13}C T_1 relaxation

In Fig. S5 are represented ^{13}C T_1 acquisitions performed with conventional NMR at $B = 7.05$ T, using the same batch of samples as in the EPR investigation in section S2.1. Acquisition was made with the NMR saturation-recovery sequence, which consists in observing the return to thermal polarization after a train of saturating pulses (here corresponding to $20 \pi/2$ pulses spaced by 5 ms). The experimental data points in Figure S5 consist of the spectrum integral at each value of the time interval between saturation and readout. Stretched exponential fits $s(t) = A \left(1 - \exp\left\{-\left(\frac{t}{T_1}\right)^\beta\right\}\right)$ are shown as dashed lines in Fig. S5 and the fitted parameters are listed in Table 2.

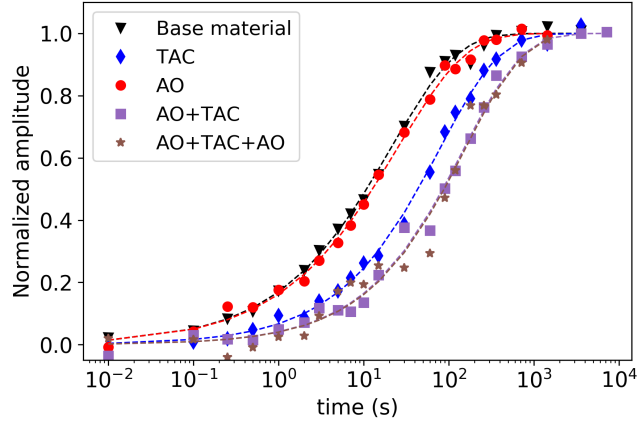


Fig. S5: ^{13}C relaxation for the 100 nm particles, at different stages of surface treatment (AO: air-oxidation, TAC: triacid-cleaning), acquired by saturation-recovery with conventional NMR at $B = 7.05$ T. Dashed lines are stretched exponential recovery fits.

100 nm sample	$^{13}\text{C} T_1$ (s)	stretch exponent β
Base material	21(1)	0.55(3)
TAC	80(4)	0.61(3)
AO	25(2)	0.54(3)
AO+TAC	152(13)	0.63(4)
AO+TAC+AO	158(37)	0.63(9)

Table 2: Fitted parameters for the ^{13}C T_1 relaxation of the 100 nm sample at different stages of surface treatment (samples are labelled as in Fig. S5).

S2.3 NV T_1 relaxation

The NV longitudinal relaxation times were measured on the 100 nm samples, that were as well electron-irradiated and annealed. Here, we compare two treatments (AO, AO+TAC). The air-oxidation (AO) was done both before and after the electron irradiation and simultaneous annealing. Triacid cleaning (for the AO+TAC sample) was performed only after the second air-oxidation. Single exponential fits of the experimental data as shown in main text, Fig. ??b provide the relaxation times given in Table 3.

In contrast to our other measurements, the magnetic field was set to the lowest at which intensity in the EPR spectrum could be detected considering the field region in main text, Fig. ??, that is, using $\nu = 9.59$ GHz, $B = 2403$ G. This allows being selective to NV centers that are aligned to the magnetic field, and avoid state-mixing induced by the misalignment. The ${}^{\text{NV}}T_1$ measured with this method reflects exclusively the rate of the single quantum transitions ($m_S = 0$ to ± 1), and thus can be compared to the typical ${}^{\text{NV}}T_1$ measurements reported in the literature. However, our determination is performed at higher magnetic field than in most cases of literature reports (using, e.g., zero-field). The increased magnetic field can lead to further decoupling of the NVs from certain noise sources, and thus favor a longer T_1 .

100 nm sample	${}^{\text{NV}}T_1$
AO	2.20(3) ms
AO + TAC	4.23(7) ms

Table 3: ${}^{\text{NV}}T_1$ corresponding to the fits shown in main text, Fig. ??b.

S2.4 XPS on smaller nanoparticles (~ 25 nm)

X-ray photoemission spectrum on a sample of 25 nm median size is shown in Fig. S6. The sample is from the same manufacturer as the 100 nm 2 μm samples (Pureon AG), however contamination induced by the fabrication process (milling) is more likely to present due to the smaller size. The Fe2p peak of iron could be detected, as shown in inset of Fig. S6. In the 100 nm sample (AO treatment), no iron could be detected by XPS, which we attribute to the lower concentration at the surface of bigger particles.

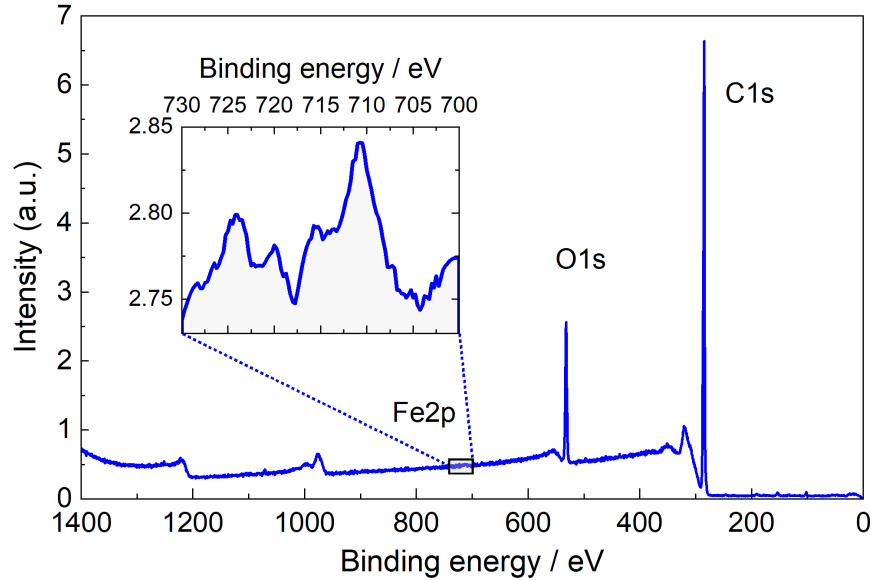


Fig. S6: X-ray photoemission spectroscopy spectrum of the sample Pureon AG, MSY0-0.5, type Ib, of 25 nm median size, showing the carbon (C1s) and oxygen (O1s) peaks. Inset: acquisition in the [700,730] eV range, showing the signal characteristic of iron (Fe2p).

S3 Sample illumination

S3.1 Illumination protocol

In contrast to single diamond crystals, the propagation of light inside of diamond powder of micro- and nanosize is hindered by strong light scattering, due to the high refractive index of diamond ($n = 2.4$ at the wavelength of 532 nm). In the context of hyperpolarization, there is a requirement to perform homogeneous optical pumping of large amounts of sample. A microstructured waveguide array was developed to ensure an efficient illumination of such quantities of diamond powder and circumvent the issue caused by light scattering.

The waveguide arrays make it possible to directly access a larger volume of micro- or nanodiamonds with light, leading to a better polarization of NV centers upon illumination.

The micro-pillar array was manufactured using a commercially available direct laser writing system, employing the 2-photon-polymerization technique (Photonic Professional GT+, Nanoscribe GmbH, Eggenstein-Leopoldshafen, Germany). We used the resin IP-S (Nanoscribe GmbH, Eggenstein-Leopoldshafen, Germany) due to its excellent optical properties in the VIS and 10x lens with NA=0.3 for fast prototyping progression. The structures were printed on a silicon wafer using the dip-in approach, where the resin acts as its own immersion medium. The slicing and hatching distances were chosen as 5 μm and 1 μm , respectively, which, although showing visible steps between layers, still produced good quality results. Uncured resin was dissolved and removed by submerging the structure in PGMEA

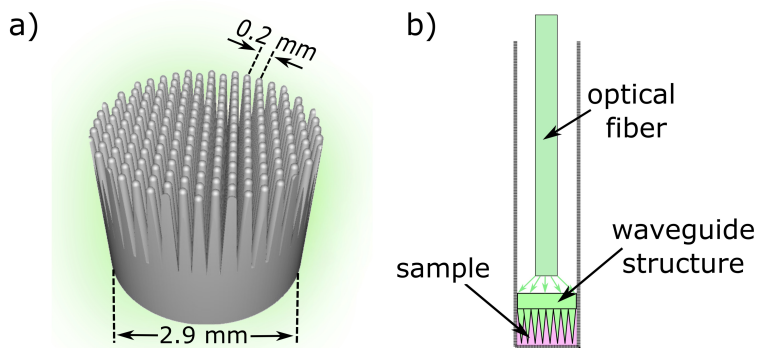


Fig. S7: a) 3D printed micro-photonic structure consisting of more than a hundred tips. b) Schematic illustration of the 3D structure inside the EPR tube, which provides optical access to the contained diamond powder.

and cleaning was done by a subsequent bath and rinsing with isopropyl alcohol during which UV curing was applied to ensure the complete polymerization of all components and to reduce shrinkage. The structure itself comprises a base with a diameter of 2.9 mm on which a hexagonal pattern of approximately 200 pillars, each around 1 mm in height, is placed. The pillars are truncated cones which are topped by a hemispherical cap (see Figure S7). The distance between the revolution axes of neighboring pillars is 200 μm .

In the sample preparation, the diamond powder was mixed with ethylcinnamat ($\text{C}_{11}\text{H}_{12}\text{O}_2$), the latter, with a refractive index ($\lambda = 532 \text{ nm}$) $n = 1.57$, has the following use for index matching 1) it reduces losses by internal reflection inside the structured array and 2) it mitigates further the effects of light scattering by the diamond particles. The mixture of diamond powder and ethylcinnamat (with a mass equal or lower to that of the diamond powder) provides a viscous fluid, which was placed in a sapphire tube of (4 mm OD, Situs Technical GmbH, Wuppertal, Germany) and the waveguide structure placed on top. As shown on Fig. S7b, an optical fiber (1.5 mm diameter) delivers the illumination. In separate trials, glycerol was used as the index-matching solution. As an alternative, water could be used, if working below the melting point. While water is in general a convenient solvent for room temperature operation, it has the issue of its strong microwave absorption above the melting point. A specific resonator design or sample geometry would be required for working with water-containing samples at room temperature.

S3.2 Phenomenological description of the NV spectrum in X-band EPR under optical pumping

S3.2.1 Redistribution of state populations

The EPR spectrum measured under illumination (as in main text, Fig. ??) shows the contribution from NV centers in randomly oriented crystallites. Therefore, all possible NV center orientations must be considered in the spectrum description.

Let us consider the case of a NV center aligned to the magnetic field. For this NV, the eigenstates, defined by the quantum number m_s , can be written as $|-1\rangle, |0\rangle, |1\rangle$. Illumination depletes equally the $|\pm 1\rangle$ states, by population transfer to $|0\rangle$, so that the occupation probability of each state (ρ_{m_s}) differs from that in thermal equilibrium. It obeys

$$\rho_{m_s} = (1 - p_{\text{NV}})\rho_{m_s,\text{thermal}} + p_{\text{NV}}|\langle m_s|0\rangle|^2, \quad (1)$$

where p_{NV} is the degree of initialization of the NV center. The $|\langle m_s|0\rangle|^2$ term equals to 1 for $m_s = 0$, and 0 otherwise. For $p_{\text{NV}} = 1$, the probability of being into the $m_s = 0$ state is maximum (100%).

When NV centers are misaligned with respect to the magnetic field, m_s no longer remains a good quantum number, due to state mixing. In this case, one can define new eigenstates $|s_{i,\theta}\rangle$, where $i = 1, 2, 3$ and θ is the angle between the NV axis and the orientation of the magnetic field. The misalignment-induced state mixing leads to different occupation probabilities compared to the aligned case. In our present phenomenological description, it is taken into account by performing the following replacement in Eq. 1:

$$|\langle m_s|0\rangle|^2 \rightarrow |\langle s_{i,\theta}|0\rangle|^2, \quad (2)$$

so that instead of Eq. 1, the occupation probability ($\rho_{i,\theta}$) of NV center to $|s_{i,\theta}\rangle$ state can be expressed as

$$\rho_{i,\theta} = (1 - p_{\text{NV}})\rho_{i,\theta,\text{thermal}} + p_{\text{NV}}|\langle s_{i,\theta}|0\rangle|^2. \quad (3)$$

In EPR, the signal is summed over each transition and scales with the population difference between the two states involved in the transition. It follows from Eq. 3 that the signal (S_{EPR}), e.g. in the field-swept spectrum, can be predicted as

$$S_{\text{EPR}} = (1 - p_{\text{NV}})S_{\text{EPR,thermal}} + p_{\text{NV}}S_{\text{EPR,pol.}}, \quad (4)$$

where $S_{\text{EPR,thermal}}$ and $S_{\text{EPR,pol.}}$ correspond respectively to thermally polarized NVs, and NVs with occupation probabilities given by $|\langle s_{i,\theta}|0\rangle|^2$ (Eq. 2).

Remarkably, the occupation probabilities predicted by this equation are strongly orientation-dependent [2]. The energy level plots in Fig. S8 illustrate the probabilities in the 0° and 90° case, calculated for $p_{\text{NV}} = 0.3$.

Although this description is of convenient use, we insist on its phenomenological character. In reality, the mechanism responsible for the change in occupation probabilities under

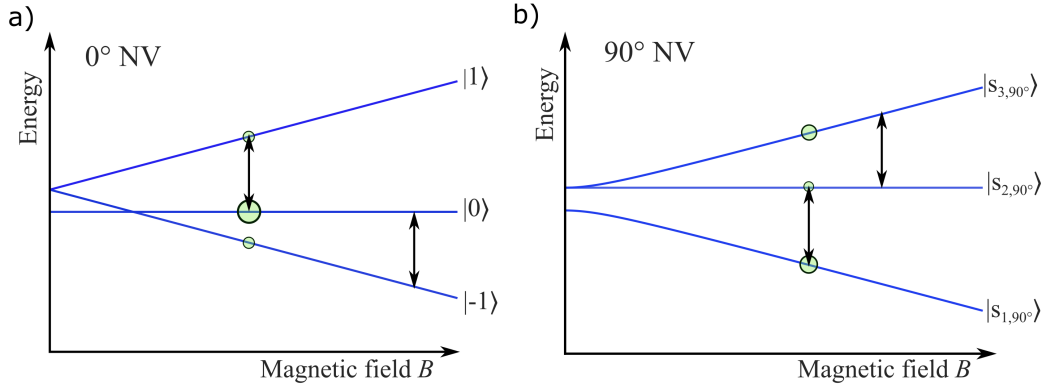


Fig. S8: Energy levels of an NV center with a) 0° and b) 90° orientation to the magnetic field. The lines represented in a) result from direct diagonalization of the Hamiltonian. The ones in b) are obtained after the derivation in section S8.1 (Eq. 26). The arrows indicate the position of the transitions in a field-swept experiment (the microwave frequency, $\nu \approx 9.6$ GHz). The diameter of the circles on the energy levels depicts the corresponding occupation probabilities under optical pumping, according to the description in section S3.2, with the parameter describing the optical initialization of the NV center in Eq. 3, $p_{\text{NV}} = 0.3$.

illumination involves the different rates in the intersystem crossing (ISC) from the ^3E excited state [3]. A complete description of the EPR spectrum under illumination should thus likely consider the change in polarization dynamics induced by state mixing within the ^3E excited state [4]. Nevertheless, the good fit of our model to the experimental data, shows that the phenomenological description already captures the main features of the spectral changes induced by illumination.

S3.2.2 Spectral fits

Simulations of the NV spectra (main text, Fig. 1 and Fig. S9) were implemented using the `pepper` in the EasySpin package in Matlab [5]. The spin system is built considering the Hamiltonian in Eq. 18. To obtain $S_{\text{EPR,thermal}}$ in Eq. 4, one can set the experiment setting `Temperature` to the wanted temperature in Kelvins (for ambient conditions, `Temperature` = 298). To obtain $S_{\text{EPR,pol}}$, the `Temperature` setting is set to `[1 0 0]` (Matlab list). When the signal is significantly enhanced above thermal ($S_{\text{EPR}}/S_{\text{EPR,thermal}} \gg 1$), as an approximation, one can keep only the second term in Eq. 4, which then yields $S_{\text{EPR}} \approx p_{\text{NV}} S_{\text{EPR,pol}}$.

Besides the orientation-induced broadening, secondary contributions to the inhomogeneous broadening of the NV center are the magnetic interaction to the surrounding spin bath (consisting of P1, other NVs, and additional paramagnetic defects), strain, and electric fields induced by local charges [6]. The interaction to the paramagnetic spin bath is consid-

ered by defining a lorentzian broadening, using the linewidth parameter lw . To take into account strain and electric fields induced by local charges -both generating center-to-center variation of e_x, e_y terms in Eq. 18- one can in fact define $e_y = 0$, and add a distribution of e_x , characterized by its full width at half maximum $FWHM(e_x)$. Indeed, since powder averaging is performed in the simulation, the e_y term need not to be considered. We approximate the distribution of the term e_x as a gaussian, which is done through the parameter $DStrain$ ($DStrain=[0,FWHM(e_x)]$). We find:

- For the 2 μm particles (main text, Fig. 1): $D = 2869$ MHz, $lw = 0.4$ mT, $FWHM(e_x) = 21$ MHz,
- For the 100 nm particles (Fig. S9): $D = 2869$ MHz, $lw = 0.4$ mT, $FWHM(e_x) = 27$ MHz,

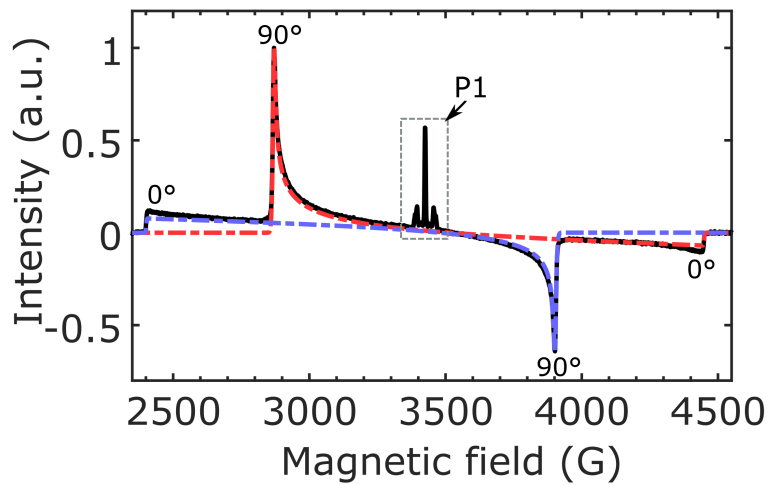


Fig. S9: NV EPR spectrum obtained after illumination with 700 μs laser pulses for 100 nm-sized nanodiamonds with a sample mass of 12 mg (black solid). The mass was subsequently decreased for hyperpolarization experiments, to ensure better illuminations conditions. Contributions from the two separate transitions fitting the experimental spectrum are represented in red and blue dashed curves, respectively.

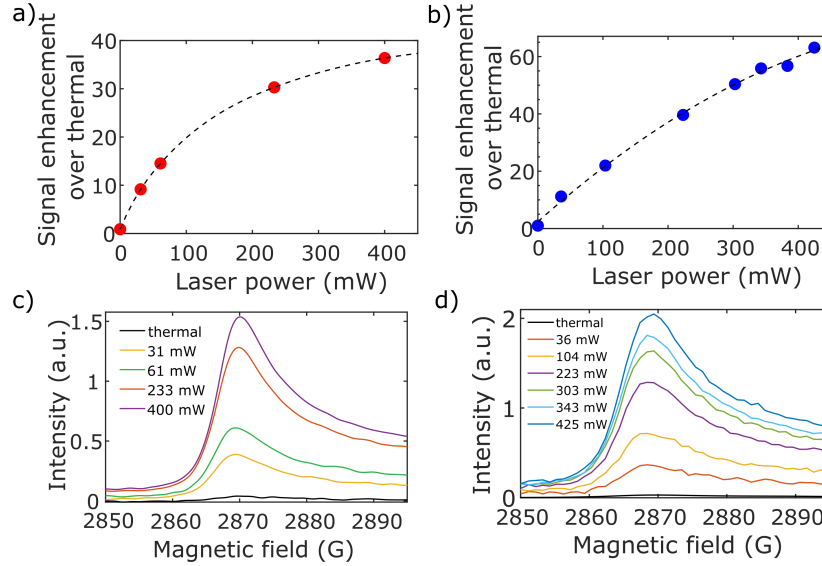


Fig. S10: Enhancement of the NV EPR signal under continuous illumination at different laser powers for the samples used for hyperpolarization (a. 2 μm , b. 100 nm). Dashed black lines are a guide to the eye. The enhancement corresponds to the intensity of the low field EPR peak corresponding to NV centers with 90° to the magnetic field, normalized to its intensity measured in the dark. Corresponding spectra are shown in c. and d. respectively.

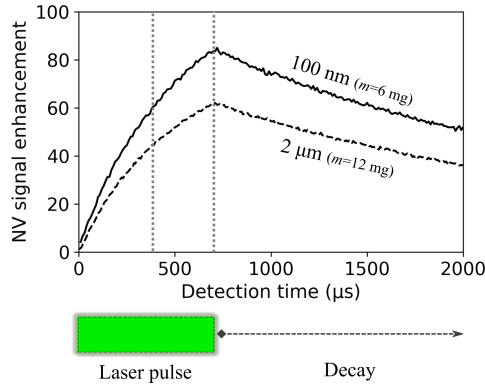


Fig. S11: Dynamics of the EPR-detected NV signal induced by a 700 μs laser pulse for the samples used in the experiments described in main text. The magnetic field is $B = 0.286$ T, and the microwave frequency $\nu = 9.58$ GHz, corresponding to the low-field peak of the Pake doublet. The experimental trace gives the enhancement of NV signal, at different times. The dotted lines indicate the laser pulse duration used in the hyperpolarization experiments reported in main text (400 μs), at which the enhancement for the 2 μm and 100 nm particles is 46 and 61 respectively, and the full length (700 μs) used in this experiment.

S3.3 Heating induced by illumination

The local temperature increase of the diamond powder sample under illumination can be calculated by considering the temperature-induced change of NV zero-field splitting D using the experimentally determined relation from Acosta et al. [7]:

$$\frac{dD}{dT} = -0.074 \text{ MHz K}^{-1}. \quad (5)$$

Combining Eq. 5 and 28, following a change in temperature ΔT , the low field NV EPR peak is expected to shift by magnetic field ΔB as follows:

$$\frac{\Delta B}{\Delta T} = \frac{dB_{12}}{dD} \frac{dD}{dT} = 0.0158 \text{ G/K}. \quad (6)$$

In this work, for precise determination of temperature changes induced by illumination, we perform the fit as detailed in section S3.2 of the EPR spectrum around the low-field peak for different values of continuous laser power (Figure S10), which provides the value of D at each laser power. Comparing to that obtained at a chosen laser power (31 mW and 100 mW for 2 μm and 100 nm, respectively), we can extract the corresponding temperature change (Fig. S12).

From the heating rates determined by the linear fits in Fig. S12, we can determine the temperature elevation of the samples during the application of the NV initialization and polarization transfer cycle described in main text, Fig. ??c. As an average laser power of 420 mW was used, the temperature changes are +51 K and +24 K for the 2 μm and 100 nm respectively.

Here, the comparatively high temperature increase for the 2 μm sample can be attributed to the two-times higher mass employed and the higher NV concentration, both increasing the heat deposition by photon absorption.

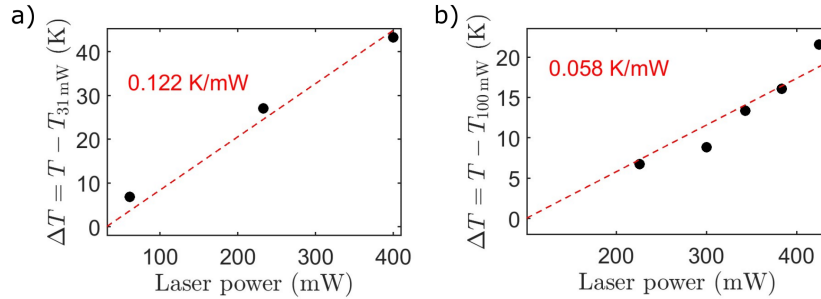


Fig. S12: Heating of the samples used in the experiments described in main text (a. 2 μm and b. 100 nm) induced by continuous illumination at different laser power. Dashed lines are a linear fits, allowing to extract as heating rates 0.122 K mW $^{-1}$ and 0.058 K mW $^{-1}$ respectively.

S3.4 Transient NV signal under pulsed illumination

To investigate the NV initialization dynamics, the evolution of the NV signal during a 700 μs laser pulse was acquired with EPR (Fig. S11). The magnetic field and frequency correspond to the transition between the two lower energy spin states, $s_{1,90^\circ}$ and $s_{2,90^\circ}$ (depicted in Fig. S8).

In the hyperpolarization experiments, shorter, 400 μs laser pulses were used. From Fig. S8, corresponding NV signal enhancements for the 2 μm and 100 nm particles, are $\epsilon_{\text{NV}} = 46$ and 61 respectively.

We now turn to the interpretation of the value of ϵ_{NV} , in terms of state occupation probabilities. The EPR signal scales with the population difference between the states involved in the transitions, and the number of centers contributing to the signal. We note here that by photoluminescence measurement, no conversion towards the neutrally charged NV^0 was observed in the samples in the used laser power range, therefore we consider the number of NV centers to be constant. In these conditions,

$$\epsilon_{\text{NV}} = \frac{(\Delta\rho)_{\text{NV}}}{(\Delta\rho)_{\text{NV,dark}}}, \quad (7)$$

where $(\Delta\rho)_{\text{NV}} = \rho_{s_1} - \rho_{s_2}$, and $(\Delta\rho)_{\text{NV,dark}} = \rho_{s_{1,\text{dark}}} - \rho_{s_{2,\text{dark}}}$, here $\rho_{s_{1,2}}$ are the occupation probabilities of states $s_{1,90^\circ}$ and $s_{2,90^\circ}$ ('90°' is omitted in the subscript for simplicity). The additional subscript 'dark' indicates the case without illumination.

In the dark, the occupation probabilities are given by the Boltzmann statistics:

$$\rho_{s_i,\text{dark}} = e^{\frac{-u_i}{kT}} / \left(\sum_{j=1}^3 e^{\frac{-u_j}{kT}} \right), \quad (8)$$

where u_i ($i = 1, 2, 3$) are the state energies given in Eq. 26. Using $D = 2869$ MHz, $B = 2860$ G, at $T = 293$ K one obtains:

$$(\Delta\rho)_{\text{NV,dark}} = \rho_{s_{1,\text{dark}}} - \rho_{s_{2,\text{dark}}} = 5.234 \times 10^{-4}. \quad (9)$$

From Eq. 9, it is straightforward to estimate the population difference as $(\Delta\rho)_{\text{NV}} = \epsilon_{\text{NV}}(\Delta\rho)_{\text{NV,dark}}$. We obtain $(\Delta\rho)_{\text{NV}} = 0.024$ and 0.032 for the 2 μm and 100 nm particles, respectively. We note that CW illumination brings similar populations in the steady-state, as comparable values of the enhancement ϵ_{NV} are observed at high laser power in Fig. S10. The determined $(\Delta\rho)_{\text{NV}}$ thus can be compared to the value ≈ 0.07 reported in NV-ensemble studies of single crystal diamonds under continuous illumination [2].

S4 Build-up and decay of ^{13}C polarization

S4.1 $2\ \mu\text{m}$ and $100\ \text{nm}$ samples, with sample rotation ($25^\circ/\text{s}$)

The build-up time, obtained from fitting the data in Figure S13 with a stretched exponential function $s(t) = A \left(1 - \exp\left\{-\left(\frac{t}{T_{\text{pol}}}\right)^\beta\right\}\right)$, is $T_{\text{pol}} = 34 \pm 2\ \text{s}$ (with $\beta = 0.85 \pm 0.06$) for the $2\ \mu\text{m}$ sample and $T_{\text{pol}} = 32 \pm 5\ \text{s}$ (with $\beta = 0.88 \pm 0.12$) for the $100\ \text{nm}$ sample. The ^{13}C spectra after buildup ($t = 300\ \text{s}$) are shown in main text, Fig. ???. The decay of polarization at 1 T, estimated from the fitting the data in Figure S13 with a single exponential decay, is $T_1 = 142 \pm 16\ \text{s}$ and $T_1 = 116 \pm 16$ for $2\ \mu\text{m}$ and $100\ \text{nm}$ diamond powders, respectively.

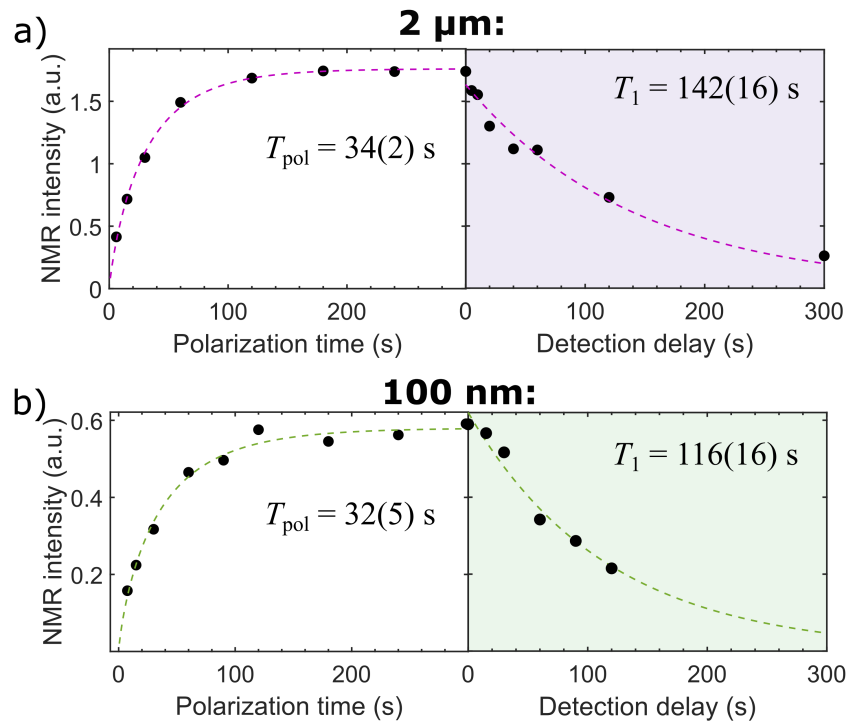


Fig. S13: Build-up (left) and decay (right) of ^{13}C polarization for a) $2\ \mu\text{m}$ and b) $100\ \text{nm}$ diamond powders, respectively. The dashed lines are the fits of the data with stretched exponential function for the build-up time and single exponential for the decay of ^{13}C polarization.

S4.2 Buildup for the 2 μm sample, without rotation

The build-up time, obtained from fitting the data in Figure S14 with a stretched exponential function is $T_{\text{pol}} = 29 \pm 4$ s (with $\beta = 0.70 \pm 0.08$).

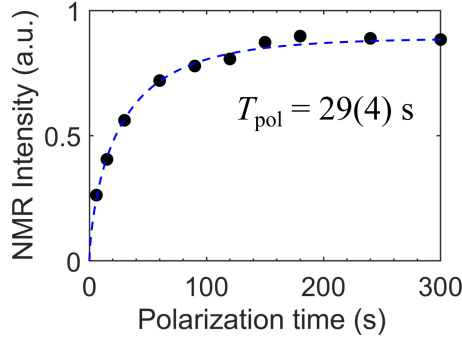


Fig. S14: Build-up of ^{13}C polarization for the 2 μm sample in the absence of sample rotation and fit with a stretched exponential function giving $T_{\text{pol}} = 29 \pm 4$ s and $\beta = 0.70 \pm 0.08$.

S5 Evaluation of the hyperpolarization enhancement factor and the absolute polarization

The signal after hyperpolarization $S_{^{13}\text{C}}$, the enhancement factor $\epsilon_{^{13}\text{C}}$ and the absolute polarization $p_{^{13}\text{C}}$ (defined in main text) obey

$$\epsilon_{^{13}\text{C}} = \frac{S_{^{13}\text{C}}}{S_{^{13}\text{C},\text{therm}}} = \frac{p_{^{13}\text{C}}}{p_{^{13}\text{C},\text{therm}}}, \quad (10)$$

where $S_{^{13}\text{C},\text{therm}}$, $p_{^{13}\text{C},\text{therm}}$ are the values of the thermal signal and the corresponding absolute nuclear polarization at thermal equilibrium.

The value of the absolute polarization at thermal equilibrium can be calculated as $p_{^{13}\text{C},\text{therm}} = \frac{\hbar\gamma_{^{13}\text{C}}B}{2k_{\text{B}}T}$, where k_{B} is the Boltzmann constant, T is the temperature, $\gamma_{^{13}\text{C}}$ is the nuclear gyromagnetic ratio (from the Boltzmann statistics as $k_{\text{B}}T \gg \hbar\gamma_{^{13}\text{C}}B$). From Eq. 10 it can be seen that, from the hyperpolarized signal, both $\epsilon_{^{13}\text{C}}$ and $p_{^{13}\text{C}}$ can be determined if the thermal signal $S_{^{13}\text{C},\text{therm}}$ can be measured. However, the sensitivity of the setup for in situ NMR detection is low and, as a result, insufficient to detect the thermal ^{13}C signal from the diamond powder samples. To address this limitation, we employed a reference sample of 40 μL water, in which the high thermal signal from the ^1H nuclei can easily be measured.

For the 2 μm particles sample, the hyperpolarized spectrum seen in main text, Fig. ??a, corresponds to a signal (observed value of the free induction decay at $t \sim 0$) of 1.407 μV

for a mass $m = 12$ mg of sample. For this sample first derive $p_{^{13}\text{C}}$ from the reference ^1H measurement in the water sample. Then we deduce $\epsilon_{^{13}\text{C}}$ at the polarization field (0.287 T).

Similar calculations apply for the 100 nm sample for which the spectrum in main text, Figure ??b corresponds to a signal of 0.441 μV for a sample mass $m = 6$ mg. For each sample, both $\epsilon_{^{13}\text{C}}$ and $p_{^{13}\text{C}}$ are reported in main text.

Determination of $p_{^{13}\text{C}}$ By measuring the intensity of the ^1H thermal signal in the water sample ($S_{^1\text{H,therm}}$), one can estimate the intensity of the ^{13}C thermal signal as follows:

$$S_{^{13}\text{C,therm}} = S_{^1\text{H,therm}}\Gamma_{\text{ref}}. \quad (11)$$

We now focus on the derivation of Γ_{ref} . The intensity of thermal signal S_{nucl} in a magnetic field B at temperature T can be estimated as [8]

$$S_{\text{nucl}} = C \times (\gamma B) \times \left(\frac{\gamma^2 \hbar^2 B N_{\text{nucl}}}{4k_{\text{B}}T} \right). \quad (12)$$

where C is a constant, determined by parameters of the detection channel, \hbar is the Planck constant, N_{nucl} is the number of detected nuclear spins, and γ is the nuclear gyromagnetic ratio. This expression is valid in the limit $k_{\text{B}}T \gg \hbar\gamma B$.

The ^{13}C signal was detected at 1.004 T. Unlike conventionally done in NMR, the detection of signals for ^1H nuclear spins was implemented at the same frequency, adjusting the magnetic field for the ^1H nucleus ($B = 0.252$ T). Therefore, it is convenient to replace the magnetic field B in equation 12, as

$$B = \frac{2\pi f}{\gamma}, \quad (13)$$

where f is the detection frequency. Furthermore, given that the measurement were both performed at ambient temperature, the ratio of thermal signals for ^1H in water and ^{13}C nuclear spins in the respective samples can be expressed as

$$\Gamma_{\text{ref}} = \frac{S_{^{13}\text{C,therm}}}{S_{^1\text{H,therm}}} = \frac{\gamma_{^{13}\text{C}} N_{^{13}\text{C}}}{\gamma_{^1\text{H}} N_{^1\text{H}}}. \quad (14)$$

The number of hydrogen and carbon nuclear spins can be estimated as follows:

$$N_{^{13}\text{C}} = \frac{m_{\text{diam.}} N_{\text{A}} C_{^{13}\text{C}}}{M_{\text{diam.}}}, N_{^1\text{H}} = \frac{n_{^1\text{H/mol}} m_{\text{water}} N_{\text{A}} C_{^1\text{H}}}{M_{\text{water}}}, \quad (15)$$

where $m_{\text{diam.}}$ and m_{water} are the masses of diamond and water samples, respectively, N_{A} is the Avogadro constant, $C_{^{13}\text{C}}$ and $C_{^1\text{H}}$ are the isotopic abundances of ^{13}C and ^1H , respectively, $n_{^1\text{H/mol}}$ is the number of hydrogen atoms per molecule ($n_{^1\text{H/mol}} = 2$), $M_{\text{diam.}}$ and M_{water} are the molar masses of water molecules and carbon in diamond at natural abundance, respectively. From the parameters listed in Table 4 we determine $\Gamma_{\text{ref}} = 1/1652$ for the 2 μm sample described in main text.

Eq. 14 and Eq. 10 yield:

sample	mass	$C_{^{13}\text{C}}$ or $C_{^1\text{H}}$	molar mass	$\gamma_{^{13}\text{C}}$ or $\gamma_{^1\text{H}}$
2 μm	12 mg	1.07%	12.011 g mol ⁻¹	$(2\pi)10.705 \text{ MHz T}^{-1}$
water reference	40 mg	99.98%	18.015 g mol ⁻¹	$(2\pi)42.576 \text{ MHz T}^{-1}$

Table 4: Sample properties used for determining the parameter Γ_{ref} , in Eq. 14, used for determination of the signal enhancement (illustrated here for the 2 μm sample).

$$p_{^{13}\text{C}} = \frac{p_{^{13}\text{C,therm}} \times S_{^{13}\text{C}}}{S_{^{13}\text{C,therm}}} = \frac{p_{^{13}\text{C,therm}} \times S_{^{13}\text{C}}}{\Gamma_{\text{ref}} \times S_{^1\text{H,therm}}} \quad (16)$$

We calculate, for the absolute thermal ^{13}C polarization at the detection field of 1.004 T ($T = 293 \text{ K}$), $p_{^{13}\text{C,thermal}} = 8.80 \times 10^{-7}$. For the reference water sample, we measure $S_{^1\text{H,therm}} = 5.420 \mu\text{V}$. Thus, for the 2 μm sample:

$$p_{^{13}\text{C}} = \frac{8.80 \times 10^{-7} \times 1.407 \mu\text{V}}{\frac{1}{1652} \times 5.420 \mu\text{V}} = 3.77 \times 10^{-4} \quad (17)$$

Similarly, for the 100 nm sample, $p_{^{13}\text{C}} = 2.36 \times 10^{-4}$ is obtained.

Determination of $\epsilon_{^{13}\text{C}}$ at the polarization field (0.287 T) For the absolute thermal ^{13}C polarization at the *polarization* field of 0.287 T ($T = 293 \text{ K}$), we calculate $p_{^{13}\text{C,thermal}} = 2.52 \times 10^{-7}$. For the 2 μm sample, it follows from Eq. 17 that: $\epsilon_{^{13}\text{C}} = \frac{p_{^{13}\text{C}}}{p_{^{13}\text{C,thermal}}} \approx 1500$. Similarly, for the 100 nm sample, we obtain $\epsilon_{^{13}\text{C}} \approx 940$.

S6 PulsePol parameter tuning

S6.1 Testing the robustness to detuning of the phase-offset PulsePol sequence

The original PulsePol sequence (main text, Fig ??a) was proposed by Schwartz *et al.* [9]. In our experiments, we however used the ‘phase-offset’ sequence described in (main text, Fig. ??b). Tratzmiller *et al.* introduced a general set of sequences based on PulsePol, in which the phase definition contains a free parameter ϕ [10]. In this definition, the original PulsePol and the sequence presently labelled ‘phase-offset’ are obtained by choosing $\phi = \pi/2$ and $\phi = 3\pi/4$, respectively.

In order to characterize the robustness to spectral detuning, we employ a single-crystal diamond, represented in Fig. S15a, that was utilized in an earlier work [11]. Addressing NV in single-crystal diamond instead of powder drastically reduces their inhomogeneous broadening, so that the sequence robustness can be tested by varying the pulse carrier frequency with respect to a group of NV transitions occupying a narrow spectral range.

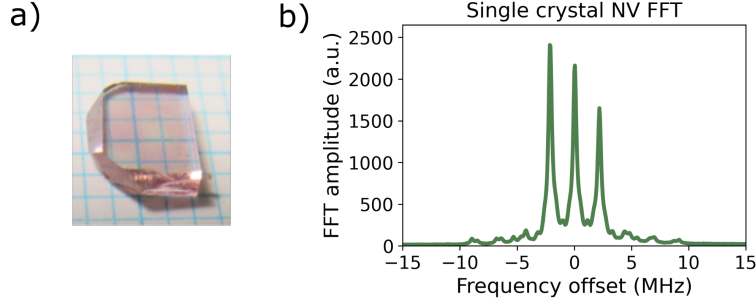


Fig. S15: a) Single crystal diamond used for the sequence robustness tests. b) Spectrum of NV around the resonator frequency $\nu = 9.7$ GHz at $B = 2436$ G aligned to the NV axis. The several lines correspond to the hyperfine structure for the $m_S = 0$ to $+1$ transition of NV. Coupling to ^{14}N nuclear spin ($I = 1$) explains the three-lines pattern, and nearby ^{13}C provide weak additional satellites. The spectrum is obtained by performing Fourier Transform of the Hahn echo signal, acquired in EPR using pulses generated by the 1 kW TWT of Rabi frequency $\Omega_1 = (2\pi)25$ MHz, under continuous illumination at $P = 100$ mW laser power.

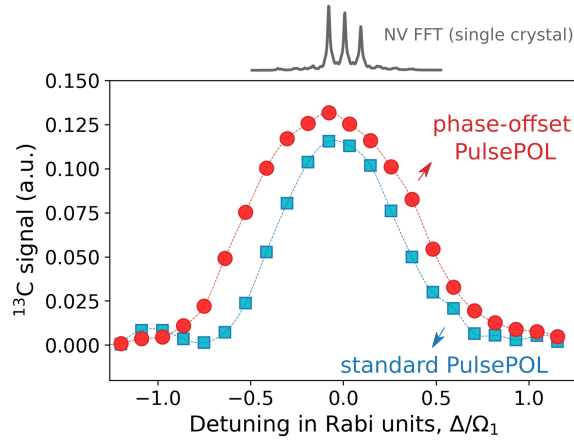


Fig. S16: Testing the robustness to detuning of the original PulsePol sequence and its variant, represented in main text Fig. ??a and ??b, respectively. ^{13}C hyperpolarized signal is acquired at different detunings Δ of the pulse carrier frequency with respect to the central line ($m_I = 0$ for ^{14}N) of the NV signal. The detuning is represented in units of the ordinary Rabi frequency $\nu_1 = \Omega_1/2\pi$. The top curve shows the FFT spectrum from Fig. S15b on the same scale. A high-power amplifier (TWT, 1 kW) was used in order to ensure a high $\nu_1 = 25$ MHz, driving the different hyperfine (^{14}N) transitions similarly. Resonance conditions $n = 3$ and $n = 3.5$ were used for PulsePol and phase-offset PulsePol respectively. The number of repetitions was $M = 10$. Lines in the main plot are a guide to the eye.

The ^{13}C signal was acquired after hyperpolarization with both the standard and phase-offset PulsePol, at different magnetic fields positively and negatively detuned from the resonance of the central hyperfine line ($m_I = 0$ for ^{14}N) visible in Fig. S15b. A change in magnetic field δB shifts the NV spectrum frequency for the central line (ν_{NV}) creating for the pulse carrier frequency (ν_{MW}) a detuning $\Delta = 2\pi(\nu_{\text{MW}} - \nu_{\text{NV}}) = -\gamma\delta B$, where Δ is given in angular frequency unit, $\gamma = (2\pi)2.8032 \text{ MHz/G}$ is the gyromagnetic ratio of the NV center. Figure S16 shows the hyperpolarized ^{13}C signal acquired with both the standard and phase-offset PulsePol. It is well visible that the latter demonstrates increased robustness to detuning, i.e. ensures the polarization transfer to be efficient in a wider spectral range.

S6.2 Comparison of resonance indices $n = 3.5$ and $n = 4.5$

In Fig. S17 is shown the simulated polarization loss of NV when applying the phase-offset PulsePol sequence for different τ intervals, considering in one case the interaction to a ^{13}C nuclear spin (Fig. S17a) and in the other case the interaction to the strongly coupled ^{14}N nuclear spin of NV (Fig. S17b).

The interaction to the ^{13}C nuclear spin leads to the expected half-integer resonances. The $n = 3.5$ and $n = 4.5$ resonances are the most intense in comparison to the other half-integer ones in the range of represented τ values. Thus the $n = 3.5$ and $n = 4.5$ resonance dips corresponds to a strong probability of transferring polarization to ^{13}C . For the chosen number of repetition of the 6-pulse block ($M = 20$ in the figure), the $n = 4.5$ resonance dip is slightly more pronounced than the $n = 3.5$ one, however this advantage should disappear if we consider the same interaction times (as a given number of repetitions is achieved in a time that is shorter by $1 - 3.5/4.5 \approx 22\%$ with the $n = 3.5$ resonance). From these considerations, i.e., assuming similar interaction times, the $n = 3.5$ resonance is expected to be advantageous.

However, the presence of the ^{14}N nuclear spin must be included and leads to more complex dynamics. This dynamics is specific to the case of NV misaligned to the magnetic field, which leads to microwave transitions affecting simultaneously the state of the ^{14}N and NV spin. These transitions, which can be predicted from the diagonalization of the Hamiltonian, are illustrated in Fig. S18. The simulation of PulsePol in Fig. S17b, which considers a NV exclusively coupled to its ^{14}N spin, shows that applying the sequence leads to a polarization loss on the NV center due to this interaction. The polarization loss on NV shows complex dependence on the parameter τ .

To prevent the interaction to ^{14}N from disturbing the dynamics of polarization transfer to ^{13}C , we choose a τ value for which the simulation predicts the polarization loss on NV induced by the NV- ^{14}N interaction to be negligible. It is visible from Fig. S17b that in the conditions of our experiment the $n = 4.5$ resonance fullfills this criterion better than the $n = 3.5$ one, therefore the former is chosen.

To confirm the benefit of using the $n = 4.5$ resonance, we performed polarization transfer at both the $n = 3.5$ and $n = 4.5$ resonances, which leads to the hyperpolarized signal seen in Figure S19 ($2 \mu\text{m}$ particles). Using the $n = 4.5$ resonance yields a 70% higher absolute signal than using the $n = 3.5$ one. This confirms the advantage of choosing the τ value

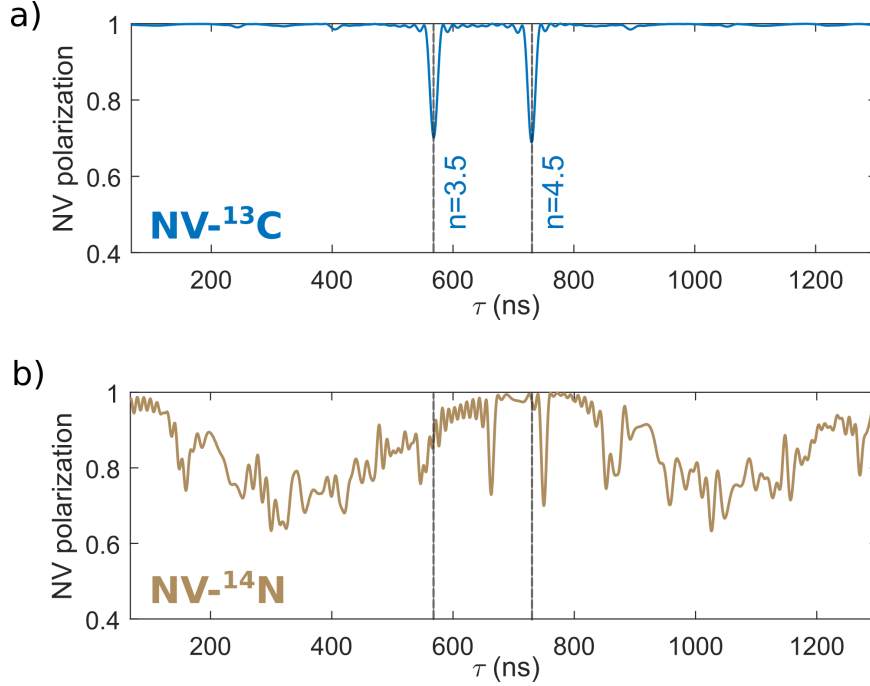


Fig. S17: Simulation of polarization dynamics for NV oriented at 90° to the magnetic field, in the conditions of our experiment ($B = 0.287$ T). The horizontal axis represents the τ delay in the sequence and the values on the vertical axis correspond to the remaining polarization of the NV, after $M = 20$ repetitions of the phase-offset PulsePol sequence. a) Case of a ^{13}C spin coupled to NV with hyperfine tensor elements $A_{ZX} = (2\pi)80$ kHz, $A_{ZY} = 0$, without interaction to ^{14}N b) Case of NV- ^{14}N interaction, where the ^{14}N Hamiltonian is taken from Felton *et al.* [12], in the absence of interaction to ^{13}C .

among available resonances so as to minimize the advert effects of the NV- ^{14}N interaction.

As the evolution dynamics of the coupled NV and ^{14}N is affected by the magnetic field, our conclusions do not hold at any value of B . At other magnetic field values, it might be favorable to use yet other phases in PulsePol (by adjusting the parameter ϕ in the general sequence definition from ref. [10]). Indeed, the resulting change in the resonance positions might allow finding conditions where the ^{14}N -related dynamics is refocused, in the same way as at our magnetic field, using the τ value corresponding to $n = 4.5$. However, the simulation of the NV- ^{14}N interaction dynamics at different magnetic fields is outside the scope of this work.

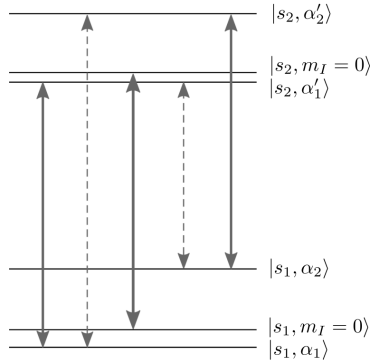


Fig. S18: Energy diagram and transitions induced by microwave on the NV center spin coupled to the ^{14}N nuclear spin for a magnetic field perpendicular to the C_{3v} symmetry axis of NV. The diagram is restricted to the low energy spin states $|s_1\rangle$ and $|s_2\rangle$ of the NV center, which were the one driven in our experiment. In this configuration the $|m_I = 0\rangle$ state of ^{14}N (choosing the axis of the applied magnetic field for quantization) is the only one that is unaffected by the hyperfine coupling to the NV. The other ^{14}N spin states are $|\alpha_1\rangle, |\alpha_2\rangle$ in the $|s_1\rangle$ manifold of NV and $|\alpha_1'\rangle, |\alpha_2'\rangle$ in the $|s_2\rangle$ manifold. The arrows represent the microwave transitions: solid for the allowed transitions, and dashed for the ‘forbidden’ transitions, respectively.

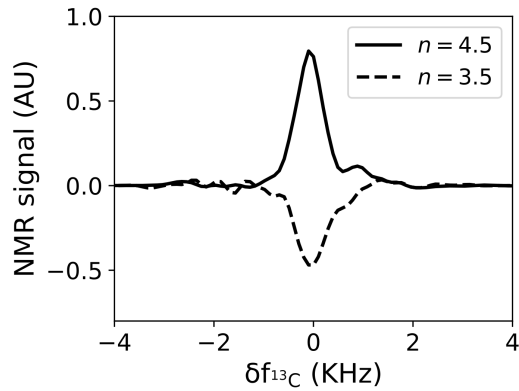


Fig. S19: Hyperpolarized signal obtained using the $n = 3.5$ and $n = 4.5$ resonances, after $M = 20$ repetitions of the phase-offset PulsePol ($2\ \mu\text{m}$ sample). The change in sign of polarization is an expected characteristic of the sequence. The signal in the case $n = 4.5$ is estimated to be 70% higher in absolute intensity than in the case $n = 3.5$.

S6.3 The composite pulses

Composite pulses consist of (quasi-)contiguous pulses of different phase and/or amplitude. This provides degrees of freedom that can be used for improving the robustness properties of sequences [13]. The composite pulses used in this work require applying microwave only on a ‘on’ or ‘off’ basis with no amplitude variation during the ‘on’ time. This makes their application of experimental convenience as one can use any microwave amplifier in its saturation regime, without the need to correct for response non-linearities.

The composite pulses used in the present work for increasing the bandwidth of PulsePol are a variant of the symmetric phase-alternating composite pulses introduced in ref. [13]: instead of analytically choosing the pulse durations in order to cancel low-order contributions from an expansion of the pulse-induced rotation in the detuning, we choose a numerical optimization which instead aims to reach a minimum fidelity threshold of the intended π -pulse in a maximal bandwidth. This can be advantageous as the additional error correction intrinsic to PulsePol loosens the constraints on the individual pulses. In order to increase the available degrees of freedom for the pulse, we allowed for non-zero waiting times between sub-pulses. A pulse description is defined via a set of durations $t_i = a_i \pi/\Omega$ written as $[a_n, \dots, a_1, a_0]$ which corresponds to a composite pulse with sub-sections of duration $(t_n, \dots, t_1, 2t_0, t_1, t_2, \dots, t_n)$ where the central t_0 durations correspond to positive-phase pulses, the odd durations $t_{2k+1, k \in \mathbb{N}}$ correspond to waiting times, and the even durations $t_{2k, k \in \mathbb{N}}$ have alternating positive and negative phase. In this notation, a non-composite rectangular π pulse is defined as [0.5]

In Table 5, the composite pulses are named by the number of pulses to each side of the central pulse (‘sidebands’), the overall duration and power of one composite pulse is measured in π pulse multiples. As there are waiting times involved, these values do not coincide. As robustness, we give the range of Δ/Ω for which PulsePol gives strong polarisation transfer (approximate values). A visual representation of the pulses, as well as the theoretical inversion profile and detuning- and robustness properties of the pulses as part of PulsePol can be found in Fig. S21.

pulse	duration	power	robustness	definition
normal	1	1	< 0.4	[0.5]
2	3.7	2.7	0.7	[0.187, 0.251, 0.408, 0.253, 0.721]
3	5.1	3.6	0.75	[0.13 0.231 0.386 0.261 0.527 0.236 0.771]
5	8.1	5.6	1	[0.167, 0.32, 0.427, 0.348, 0.658, 0.263, 0.72, 0.292, 0.822]

Table 5: Overview over definitions and properties of the numerically optimized phase-alternating composite pulses of which the 2-sideband pulse was used in this work to increase the bandwidth of PulsePol. The values for robustness here refer to the range of detunings Δ in which polarisation transfer remains successful, such that value of 1 corresponds to the bandwidth $\Delta \in [-1\Omega, +1\Omega]$ (cf. Fig. S21).

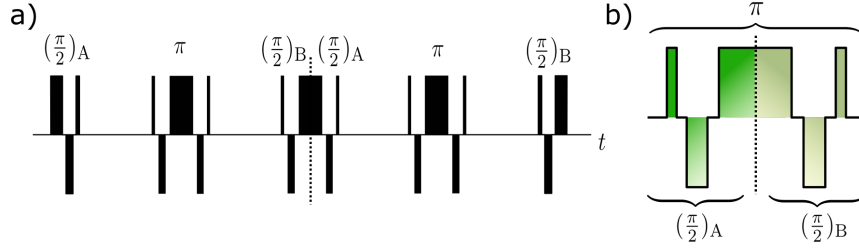


Fig. S20: a) Illustration of the PulsePol sequence, where composite pulses with two sidebands replace rectangular pulses. b) Central pulse, consisting of two types of $\pi/2$ pulses, of symmetric shape.

In our experiments, the two-sideband pulse was used, with Rabi $\Omega_1 = (2\pi)10.5$ MHz. It can be seen from Table 5 that the width of the range of detunings for which PulsePol gives strong polarization transfer is $\Delta_{\text{pol}} = 1.4\Omega_1 = (2\pi)14.7$ MHz.

As derived in [13], the symmetry of the composite π -pulses implies that they are constant-phase pulses over their respective bandwidth, as well as that the left and right halves of the pulses are broadband z -to- x and x -to- z point-to-point rotations for the left and right half of the pulse, respectively. These properties make these composite pulses well-suited for the application in PulsePol, as the $(\pi/2)_X - (\pi)_Y - (\pi/2)_X$ combination can play out its full error correction for small deviations of the optimal rotation. Furthermore, the oscillatory behavior of the sidebands of phase-alternating pulses makes it possible to fill a relatively large fraction of the waiting times of PulsePol without significantly degrading transfer properties.

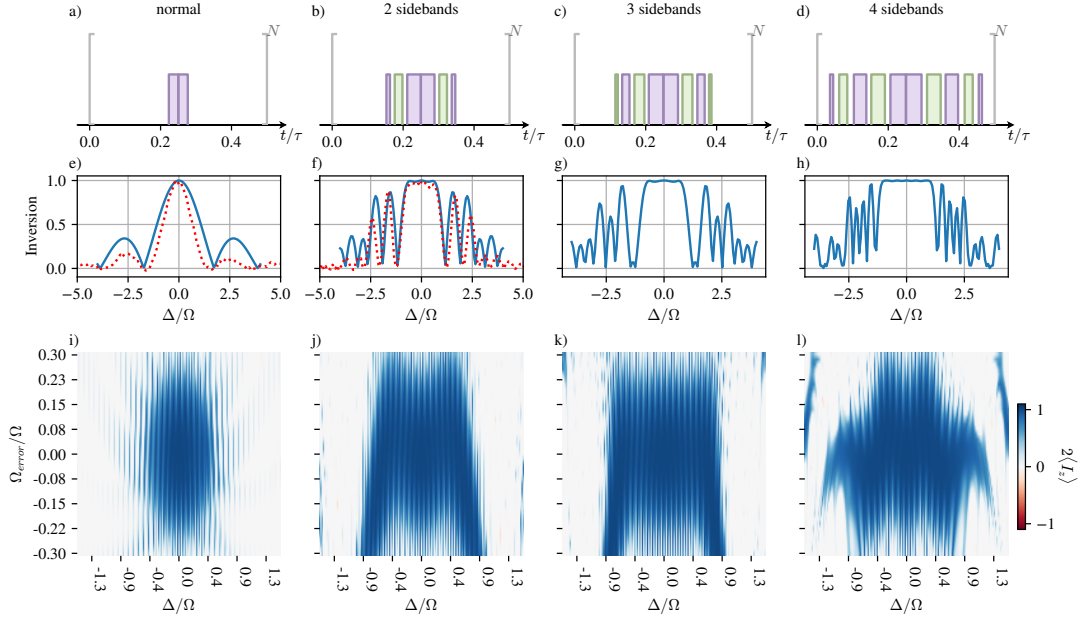


Fig. S21: Composite pulses (a–d), theoretical (solid line) and experimental (dotted line where available) inversion properties (e–h), both assuming the experimental Rabi frequency with $\pi/\Omega = 48$ ns; and pulse-error robustness properties as part of PulsePol using an increased Rabi frequency of $\Omega = (2\pi) 30$ MHz to allow for also using the longer composite pulses (i–l). Thus, (a,e,i) correspond to the standard rectangular pulse, (b,f,j) to the 2-sideband pulse, (c,g,k) to the 3-sideband pulse, and (d,h,l) to the 4-sideband composite pulse. The experimental profiles appearing as dotted lines in (e,f) were taken on NVs aligned to the magnetic field, in the single crystal diamond also used for experiments described in section S6.1.

S6.4 Other parameters adjustment

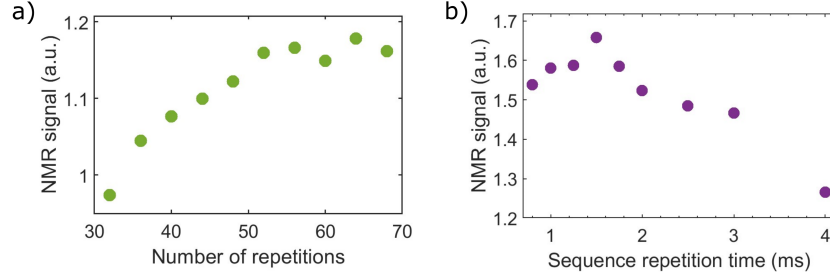


Fig. S22: Hyperpolarized ^{13}C NMR signals for the $2\ \mu\text{m}$ sample a) as a function of the number of repetitions M in the PulsePol sequence, using sequence repetition time $\tau_{\text{SRT}} = 1.5\ \text{ms}$ b) as a function of the sequence repetition time τ_{SRT} , using $M = 68$. To mitigate sample heating in b), the length of the laser initialization pulse was varied to ensure constant laser duty cycle, as $t_{\text{laser}} = \frac{400\ \mu\text{s}}{1500\ \mu\text{s}} \times \tau_{\text{SRT}}$.

S7 Potential adaptations for further increase of the bandwidth Δ_{pol}

Using a higher power amplifier. In our experiments, we used a 40 W microwave amplifier for applying the polarization transfer sequences, and obtained $\Delta_{\text{pol}} = (2\pi)15\ \text{MHz}$. Using a higher power amplifier (500 W) would ensure $\Delta_{\text{pol}} \approx (2\pi)50\ \text{MHz}$ without change in the protocol.

Sequence multiplexing. For further improvement, one could also use pulses fulfilling two criteria, that is not only performing efficient driving in a defined spectral range, but also leaving the spin polarization essentially unaffected outside this region. Although our approach based on composite pulses enabled us to meet the first criterion, it did not fulfill the second. However, one could possibly resort to envelope-modulated pulses [14, 15]. Despite their application being experimentally more involved (as they requires good control over the non-linearities in the amplifier and the excitation channel overall) compared to our composite pulses, they would enable applying the polarization sequence at nearby frequencies (this is in fact comparable to the idea of applying parallel sweeps, i.e. frequency combs in the ISE [16]). The frequency selectivity of the pulse would mitigate the advert effects of multiplexing, i.e. cross-talks.

We expect that this approach could extend further the proportion of addressed NVs, leading to $\Delta_{\text{pol}} = (2\pi)100\ \text{MHz}$. The simulation shows that this corresponds to a 16% fraction of addressed NVs. To make implementation more straightforward and for ensuring

faster polarization transfer, the frequency multiplexing and the use of the high power amplifier could be combined.

S8 NV spin Hamiltonian

In this section, we consider the NV spin Hamiltonian and derive properties related to experiments done in diamond powder, where all NV orientations are present, under a magnetic field.

First, we recall that the spin Hamiltonian for NV in an external magnetic field \mathbf{B} is given by (neglecting the ^{14}N and ^{13}C hyperfine terms)

$$\hat{H}/h = D\hat{S}_z^2 + \bar{\gamma}\mathbf{B} \cdot \hat{\mathbf{S}} + e_x(\hat{S}_y^2 - \hat{S}_x^2) + e_y(\hat{S}_x\hat{S}_y + \hat{S}_y\hat{S}_x), \quad (18)$$

where D is the zero-field splitting of the NV center, z is the defect axis, $\bar{\gamma} = \gamma/2\pi$ (γ is the gyromagnetic ratio of NV), e_x and e_y are terms related to strain and local charges [6].

S8.1 Spin Hamiltonian diagonalization for NV centers under transverse B -field

Hyperpolarization of nuclear spins was implemented by using NV centers oriented with 90° to the magnetic field. In this section, we will describe the diagonalization of the spin Hamiltonian of NV centers with 90° orientation to the magnetic field, which allows deriving analytically the position of the resonance peaks in the field-swept spectrum. The obtained results are used in section S3.3, to predict the shift in the magnetic field of the 90° resonance (low field) following a change in D , induced by heating.

For diagonalization, we follow steps that have already been described in the literature [17, 18]. For simplicity, we now assume $e_x, e_y \approx 0$ in Eq. 18, as the variation of the EPR line position with the temperature, originates dominantly from the change in D . The Hamiltonian in Eq. 18 becomes

$$\hat{H}/h \approx D\hat{S}_z^2 + \bar{\gamma}\mathbf{B} \cdot \hat{\mathbf{S}}. \quad (19)$$

Let's now assume a magnetic field B is applied along x perpendicular to the axis of the NV. In this scenario, the Hamiltonian in Eq. 19 transforms into

$$\hat{H}/h = D\hat{S}_z^2 + \bar{\gamma}B\hat{S}_x, \quad (20)$$

where the operators \hat{S}_z and \hat{S}_x in Eq. 20 are the spin matrices:

$$\hat{S}_z = \begin{pmatrix} 1 & 0 & 0 \\ 0 & 0 & 0 \\ 0 & 0 & -1 \end{pmatrix}, \quad \hat{S}_x = \frac{1}{\sqrt{2}} \begin{pmatrix} 0 & 1 & 0 \\ 1 & 0 & 1 \\ 0 & 1 & 0 \end{pmatrix}. \quad (21)$$

In the basis of the zero-field eigenstates $| -1 \rangle$, $| 0 \rangle$, $| 1 \rangle$, the 90° NV Hamiltonian can be expressed as

$$\hat{H}/h = \begin{pmatrix} D & \frac{\bar{\gamma}B}{\sqrt{2}} & 0 \\ \frac{\bar{\gamma}B}{\sqrt{2}} & 0 & \frac{\bar{\gamma}B}{\sqrt{2}} \\ 0 & \frac{\bar{\gamma}B}{\sqrt{2}} & D \end{pmatrix}. \quad (22)$$

In order to find energies, we must diagonalize NV Hamiltonian:

$$\det(\hat{H}/h - u) = 0, \quad (23)$$

$$\left| \begin{pmatrix} D-u & \frac{\bar{\gamma}B}{\sqrt{2}} & 0 \\ \frac{\bar{\gamma}B}{\sqrt{2}} & -u & \frac{\bar{\gamma}B}{\sqrt{2}} \\ 0 & \frac{\bar{\gamma}B}{\sqrt{2}} & D-u \end{pmatrix} \right| = 0, \quad (24)$$

$$-u(D-u)^2 - 2(D-u)\left(\frac{\bar{\gamma}B}{\sqrt{2}}\right)^2 = 0. \quad (25)$$

The solutions of equation 25 are

$$u_1 = \frac{D - \sqrt{D^2 + (2\bar{\gamma}B)^2}}{2}, \quad u_2 = D, \quad u_3 = \frac{D + \sqrt{D^2 + (2\bar{\gamma}B)^2}}{2}. \quad (26)$$

The corresponding dependency of energies versus magnetic field is shown in Fig. S8b. EPR spectra are typically obtained by sweeping a magnetic field at a constant microwave frequency ν . The resonance magnetic fields B_{12} and B_{23} , corresponding to the transitions $u_2 \rightarrow u_1$ and $u_3 \rightarrow u_2$, are calculated as

$$B_{12} = \frac{1}{\bar{\gamma}} \sqrt{\nu(\nu - D)}, \quad B_{23} = \frac{1}{\bar{\gamma}} \sqrt{\nu(\nu + D)}. \quad (27)$$

The change of the low field 90° NV resonance line position (for use in section S3.3) can be written as a function of D as

$$\frac{dB_{12}}{dD} = \frac{-\nu}{2\bar{\gamma}\sqrt{\nu^2 - D\nu}} = -0.213 \text{ G/MHz}, \quad (28)$$

taking $\nu = 9.6$ GHz, $D = 2869$ MHz, $\bar{\gamma} = 2.8032$ MHz/G.

The eigenstates corresponding to the energies in Eq. 26 are:

$$\begin{aligned} |s_{1,90^\circ}\rangle &= \frac{1}{\sqrt{1+c^2}} \left(|0\rangle + c \frac{|-1\rangle + |+1\rangle}{\sqrt{2}} \right) \\ |s_{2,90^\circ}\rangle &= \frac{|+1\rangle - |-1\rangle}{\sqrt{2}} \\ |s_{3,90^\circ}\rangle &= \frac{1}{\sqrt{1+c'^2}} \left(|0\rangle + c' \frac{|-1\rangle + |+1\rangle}{\sqrt{2}} \right), \end{aligned} \quad (29)$$

with $c = \frac{D - \sqrt{(D/2)^2 + (\bar{\gamma}B)^2}}{\bar{\gamma}B}$ and $c' = \frac{D + \sqrt{(D/2)^2 + (\bar{\gamma}B)^2}}{\bar{\gamma}B}$. At $B = 0.287$ T, one has $c = -0.8375$ and $c' = 1.1941$.

S8.2 Fraction of NV centers in the bandwidth Δ_{pol} ($\approx 90^\circ$ to the magnetic field)

We derive the condition for NV with an axis that is slightly misaligned from the perpendicular condition, i.e. at an angle $90^\circ + \delta$ from the magnetic field, to be present in the active bandwidth of the polarization sequence, Δ_{pol} .

In the frame of the NV center x, y, z , the magnetic field can be written as $\mathbf{B} = (B \cos(\delta), 0, B \sin(\delta))$. In fact, the effect of the tilt in the magnetic field can be treated considering the change in the magnetic field vector $\mathbf{b} = (b_\perp, 0, b_\parallel) \approx B(-\delta^2/2, 0, \delta)$. We solve the Hamiltonian in the basis of the eigenstates for the exact, 90° tilt of the magnetic field to the NV axis, which were determined previously in section S8.1.

$$\left| \begin{pmatrix} u_1 + \frac{2c}{1+c^2} \bar{\gamma} b_\perp - u' & \frac{c}{\sqrt{1+c^2}} \bar{\gamma} b_\parallel & \frac{c+c'}{\sqrt{(1+c^2)(1+c'^2)}} \bar{\gamma} b_\perp \\ \frac{c}{1+c^2} \bar{\gamma} b_\parallel & u_2 - u' & \frac{c'}{1+c'^2} \bar{\gamma} b_\parallel \\ \frac{c+c'}{\sqrt{(1+c^2)(1+c'^2)}} \bar{\gamma} b_\perp & \frac{c'}{1+c'^2} \bar{\gamma} b_\parallel & u_3 + \frac{2c'}{1+c'^2} \bar{\gamma} b_\perp - u' \end{pmatrix} \right| = 0,$$

where $u_i, i = 1, 2, 3$ are the energies in Eq. 26 and c, c' are the magnetic field-dependent terms defined in section S8.1, u' is the variable to be determined.

Restricting to the terms up to the second order in δ , the new energies read

$$u'_1 = u_1 - \bar{\gamma} B \left[\frac{c}{1+c^2} + \frac{c^2}{1+c^2} \frac{\bar{\gamma} B}{u_2 - u_1} \right] \delta^2 = u_1 + \frac{D}{2} \left(1 - \frac{D}{\sqrt{D^2 + (2\bar{\gamma} B)^2}} \right) \delta^2, \quad (30)$$

$$u'_2 = u_2 + \bar{\gamma} B \left[\frac{c^2}{1+c^2} \frac{\bar{\gamma} B}{u_2 - u_1} - \frac{c'^2}{1+c'^2} \frac{\bar{\gamma} B}{u_3 - u_2} \right] \delta^2 = u_2 - D \delta^2, \quad (31)$$

$$u'_3 \approx u_3 + \bar{\gamma} B \left[+ \frac{c'^2}{1+c'^2} \frac{\bar{\gamma} B}{u_3 - u_2} - \frac{c'}{1+c'^2} \right] \delta^2 = u_3 + \frac{D}{2} \left(1 + \frac{D}{\sqrt{D^2 + (2\bar{\gamma} B)^2}} \right) \delta^2. \quad (32)$$

We now consider the transition $|s_1\rangle \rightarrow |s_2\rangle$ between the states of energy u'_1 and u'_2 at $B = 0.287$ T. The transition frequency $\nu'_{12} = u'_2 - u'_1$, varies with the tilt δ so that

$$\nu'_{12} \approx \nu_{12} - (4052 \text{ MHz}) \times \delta^2, \quad (33)$$

where $\nu_{12} = u_2 - u_1$. Now taking into account the width (here in ordinary frequency) $\Delta_{\text{pol}}/2\pi = 15$ MHz, it is possible to cover all the NV centers for which

$$|\delta| < \delta_M = \sqrt{\frac{15}{4052}} = 0.0608 \text{ rad} \quad [3.48^\circ]. \quad (34)$$

The fraction of NV centers that is addressed is the covered portion of the solid angle, that is exactly δ_M . This suggests that 6.08 % of NV centers are within the bandwidth Δ_{pol} .

However, this calculation neglects the inhomogeneous broadening from sources other than the orientation-dependence of the transition frequency. Including the additional sources of inhomogeneous broadening, determined from the spectral fits (section S3.2), we find from a numerical simulation that the fraction of NV centers is **4.15 %** for the $|s_1\rangle \rightarrow |s_2\rangle$ transition. The other transition $|s_2\rangle \rightarrow |s_3\rangle$ contributes by a small amount, **0.21 %**. Thus we keep $\approx 4\%$ as the number of NV addressed by the polarization sequence, in the 15 MHz bandwidth, and correspondingly $\delta_M = 0.04 \text{ rad} \sim 2.5^\circ$.

S8.3 NV transition dipole and Rabi inhomogeneity

The different orientations of the nanocrystals leads to a variation of the magnetic transition dipole, even if the orientation of the NV center to the external magnetic field is fixed ($\approx 90^\circ$ in our experiments). It is possible to derive the corresponding inhomogeneity of the Rabi frequency for NV centers. For a linearly polarized microwave field and a transition between two states $|s_i\rangle$, and $|s_j\rangle$, the transition dipole can be expressed as

$$d_{ij} = \langle s_i | \hat{S}_1 | s_j \rangle, \quad (35)$$

where \hat{S}_1 is the projection on the spin-operator in the direction of the linearly polarized \mathbf{B}_1 -field. In our configuration (EPR resonator), the \mathbf{B}_1 -field is perpendicular to the static magnetic field \mathbf{B} . Using the coordinate system in Fig. S23a, it follows that $\hat{S}_1 = \cos \phi \hat{S}_z + \sin \phi \hat{S}_y$.

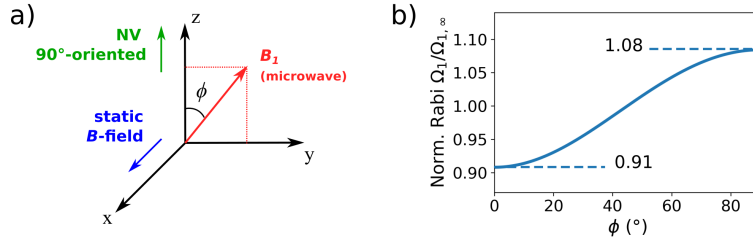


Fig. S23: a) Coordinate system of the NV frame, in the case of a perpendicular magnetic field ($\parallel x$), and definition of the orientation of the linearly polarized microwave field (in yz plane). b) Rabi vs ϕ angle for the employed $|s_1\rangle \rightarrow |s_2\rangle$ transition of NV at $B = 0.287 \text{ T}$ after normalization to the Rabi frequency $\Omega_{1,\infty}$ obtained in the high-field regime ($\bar{\gamma}B \gg D$).

Considering the 90° -oriented NV centers and the transitions between the states $|s_1\rangle$ and $|s_2\rangle$, using Eq. 29 we obtain: $d_{12} = (c \cos(\phi) + i \sin(\phi)) / \sqrt{1 + c^2}$, where c is the magnetic-field dependent term defined in section S8.1. As $c < 1$, The magnitude of d_{12} is the weakest when the microwave field points in the direction of the axis (z) of the NV center, and the strongest when it is directed along y (as $c' > 1$, the situation is however reverted for the other transition). It is straightforward to derive the Rabi frequency, as it obeys $\Omega_1 \propto |d_{12}|$. One can write

$$\frac{\Omega_1}{\Omega_{1,\infty}} = \frac{\sqrt{c^2 \cos^2(\phi) + \sin^2(\phi)}}{\sqrt{1 + c^2}} \quad (36)$$

where $\Omega_{1,\infty}$ is the Rabi frequency assuming the Zeeman eigenstates (obtained for $B \gg D$: $c \rightarrow 1$ and therefore $d_{12} = 1/\sqrt{2}$).

At $B = 0.287$ T, the values of $\Omega_1/\Omega_{1,\infty}$ vary in the range $[0.91, 1.08]$ (Fig. S23b). Roughly speaking, the Rabi frequency has variations included within a $\pm 10\%$ range at this magnetic field.

S8.4 NV transition frequencies in diamond powder at different magnetic fields

The distribution of transition frequencies in randomly oriented NV ensembles is shown in Figure S24a for the main NV transitions. The simulation was performed with Easyspin. In contrast with the simulation described in section S3.2, the setting **Temperature** was not defined (to give equal positive weight to both transitions) and the optional setting **Intensity** was set to **Off** (to remove the effect of varying transition dipoles as a function of the orientation).

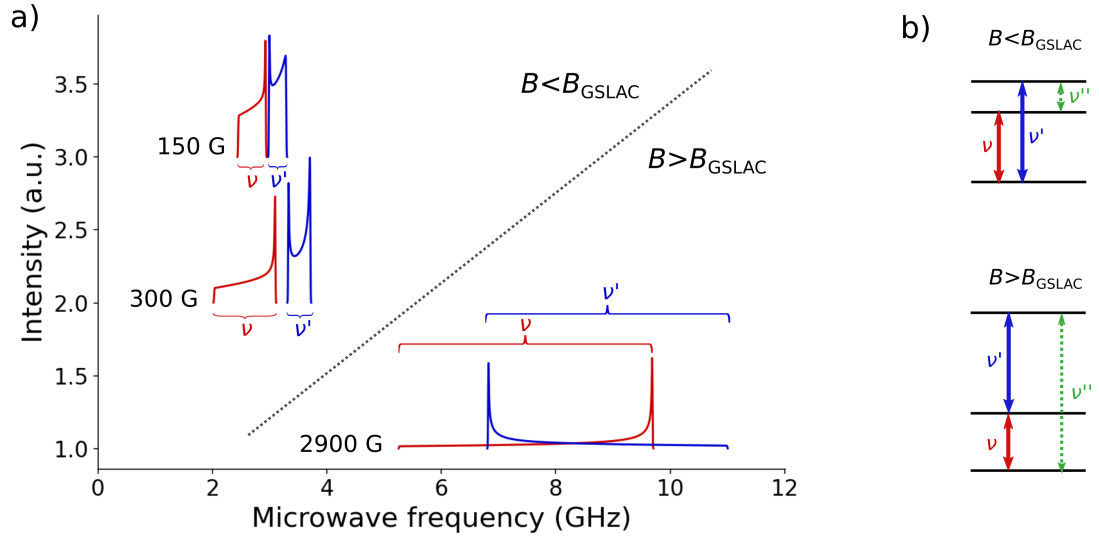


Fig. S24: a) Simulation of the distribution of the transition frequencies of NV in diamond powder at magnetic fields $B = 150$ G, 300 G and 2900 G. The frequencies ν, ν' correspond to the transitions as defined in b), where B_{GSLAC} is the magnetic field of the ground state level anticrossing ($B_{\text{GSLAC}} \sim 1024$ G). The spectrum for the transition at ν'' (dotted arrows) is not represented in a) (see text).

Besides the transitions represented in Figure S24a, we indicate a third transition in

Figure S24b (at frequency ν''). In the case of a magnetic field aligned to the NV axis, the transition is known as double quantum ($-1 \leftrightarrow +1$), and has vanishing dipole. In the case of a magnetic field tilted from the NV axis, this third transition can be excited as a single quantum transition, owing to spin state mixing. At the considered magnetic fields, however, the corresponding dipole is typically lower than that of the other transitions, thus it was not represented in the spectrum in Figure S24a

References

- [1] B. V. Yavkin, G. V. Mamin, M. R. Gafurov, and S. B. Orlinskii. Size-dependent concentration of N0 paramagnetic centres in HPHT nanodiamonds. *Magn. Reson. Solids*, 17:15101, 2015.
- [2] M. Drake, E. Scott, and J. A. Reimer. Influence of magnetic field alignment and defect concentration on nitrogen-vacancy polarization in diamond. *New Journal of Physics*, 18(1):013011, dec 2015.
- [3] M. L. Goldman, M. W. Doherty, A. Sipahigil, N. Y. Yao, S. D. Bennett, N. B. Manson, A. Kubanek, and M. D. Lukin. State-selective intersystem crossing in nitrogen-vacancy centers. *Physical Review B*, 91(16), April 2015.
- [4] J.-P. Tetienne, L. Rondin, P. Spinicelli, M. Chipaux, T. Debuisschert, J.-F. Roch, and V. Jacques. Magnetic-field-dependent photodynamics of single NV defects in diamond: an application to qualitative all-optical magnetic imaging. *New Journal of Physics*, 14(10):103033, October 2012.
- [5] S. Stoll and A. Schweiger. EasySpin, a Comprehensive Software Package for Spectral Simulation and Analysis in EPR. *J. Magn. Reson.*, 178(1):42–55, 2006.
- [6] T. Mittiga, S. Hsieh, C. Zu, B. Kobrin, F. Machado, P. Bhattacharyya, N. Z. Rui, A. Jarmola, S. Choi, D. Budker, and N. Y. Yao. Imaging the local charge environment of nitrogen-vacancy centers in diamond. *Physical Review Letters*, 121(24), December 2018.
- [7] V. M. Acosta, E. Bauch, M. P. Ledbetter, A. Waxman, L.-S. Bouchard, and D. Budker. Temperature Dependence of the Nitrogen-Vacancy Magnetic Resonance in Diamond. *Phys. Rev. Lett.*, 104:070801, Feb 2010.
- [8] Andrew Webb. Increasing the Sensitivity of Magnetic Resonance Spectroscopy and Imaging. *Analytical Chemistry*, 84(1):9–16, 2012. PMID: 21978101.
- [9] Ilai Schwartz, Jochen Scheuer, Benedikt Tratzmiller, Samuel Müller, Qiong Chen, Ish Dhand, Zhen-Yu Wang, Christoph Müller, Boris Naydenov, Fedor Jelezko, and Martin B. Plenio. Robust optical polarization of nuclear spin baths using Hamiltonian engineering of nitrogen-vacancy center quantum dynamics. *Science Advances*, 4(8), 2018.

- [10] Benedikt Tratzmiller, Jan F. Haase, Zhenyu Wang, and Martin B. Plenio. Parallel selective nuclear-spin addressing for fast high-fidelity quantum gates. *Physical Review A*, 103(1), jan 2021.
- [11] J. Scheuer, I. Schwartz, Q. Chen, D. Schulze-Sünninghausen, P. Carl, P. Höfer, A. Retzker, H. Sumiya, J. Isoya, B. Luy, M. B. Plenio, B. Naydenov, and F. Jelezko. Optically induced dynamic nuclear spin polarisation in diamond. *New Journal of Physics*, 18(1):013040, January 2016.
- [12] S. Felton, A. M. Edmonds, M. E. Newton, P. M. Martineau, D. Fisher, D. J. Twitchen, and J. M. Baker. Hyperfine interaction in the ground state of the negatively charged nitrogen vacancy center in diamond. *Phys. Rev. B*, 79:075203, Feb 2009.
- [13] A.J Shaka and A Pines. Symmetric phase-alternating composite pulses. *Journal of Magnetic Resonance (1969)*, 71(3):495–503, 1987.
- [14] D. J. Lurie. A systematic design procedure for selective pulses in NMR imaging. *Magnetic Resonance Imaging*, 3(3):235–243, 1985.
- [15] Kyryl Kobzar, Sebastian Ehni, Thomas E. Skinner, Steffen J. Glaser, and Burkhard Luy. Exploring the limits of broadband 90° and 180° universal rotation pulses. *Journal of Magnetic Resonance*, 225:142–160, 2012.
- [16] A. Ajoy, R. Nazaryan, K. Liu, X. Lv, B. Safvati, G. Wang, E. Druga, J. A. Reimer, D. Suter, C. Ramanathan, C. A. Meriles, and A. Pines. Enhanced dynamic nuclear polarization via swept microwave frequency combs. *Proceedings of the National Academy of Sciences*, 115(42):10576–10581, oct 2018.
- [17] F. E. Mabbs and D. Collison. *Electron paramagnetic resonance of d transition metal compounds*. Elsevier, 2013.
- [18] Boris Yavkin, Marat Gafurov, Mikhail Volodin, Georgy Mamin, and Sergei B. Orlinskii. EPR and double resonances in study of diamonds and nanodiamonds. In *Experimental Methods in the Physical Sciences*, pages 83–113. Elsevier, 2019.